74N12092

NASA TECHNICAL NOTE **NASA TN D-7429**

NASA TN D-7429

MEASURED PRESSURE DISTRIBUTIONS ON LARGE-ANGLE CONES IN HYPERSONIC FLOWS OF TETRAFLUOROMETHANE, AIR, AND HELIUM

by Robert A. Jones and James L. Hunt
Langley Research Center
Hampton, Va. 23665

NATIONAL AERONAUTICS AND SPACE ADMINISTRATION • WASHINGTON, D. C. • DECEMBER 1973

1. Report No. NASA TN D-7429	2. Government Accession No.	3. Recipient's Catalog No.
4. Title and Subtitle MEASURED PRESSURE DISTRIBUTIONS ON LARGE-ANGLE CONES IN HYPERSONIC FLOWS OF TETRAFLUOROMETHANE, AIR, AND HELIUM		5. Report Date December 1973 6. Performing Organization Code
7. Author(s) Robert A. Jones and James L. Hunt		8. Performing Organization Report No. L-8834
9. Performing Organization Name and Address NASA Langley Research Center Hampton, Va. 23665		10. Work Unit No. 502-37-01-10 11. Contract or Grant No.
12. Sponsoring Agency Name and Address National Aeronautics and Space Administration Washington, D.C. 20546		13. Type of Report and Period Covered Technical Note 14. Sponsoring Agency Code

15. Supplementary Notes

16. Abstract

An experimental study of surface pressure distributions on a family of blunt and sharp large angle cones was made in hypersonic flows of helium, air, and tetrafluoromethane. The effective isentropic exponents of these flows were 1.67, 1.40, and 1.12. Thus, the effect of large shock density ratios such as might be encountered during planetary entry because of "real-gas" effects could be studied by comparing results in tetrafluoromethane with those in air and helium. It was found that shock density ratio had a large effect on both shock shape and pressure distribution. The differences in pressure distribution indicate that for atmospheric flight at high speed where "real-gas" effects produce large shock density ratios, large-angle cone vehicles can be expected to experience different trim angles of attack, drag coefficient, and lift-drag ratios than those for ground tests in air wind tunnels. Comparison of the data with several theories indicated that (1) for sharp cones having attached shock waves, the sharp-cone solutions provide a good prediction of pressure, and (2) for both sharp and blunt cones having subsonic flow over the forebody, the semiempirical, sin^2-deficiency method of Love gave the best prediction of pressure distribution.

17. Key Words (Suggested by Author(s)) Real-gas effects Pressure distributions High-drag configurations	18. Distribution Statement Unclassified – Unlimited

19. Security Classif. (of this report) Unclassified	20. Security Classif. (of this page) Unclassified	21. No. of Pages 58	22. Price* Domestic, $3.50 Foreign, $6.00

*For sale by the National Technical Information Service, Springfield, Virginia 22151

MEASURED PRESSURE DISTRIBUTIONS ON LARGE-ANGLE CONES IN HYPERSONIC FLOWS OF TETRAFLUOROMETHANE, AIR, AND HELIUM

By Robert A. Jones and James L. Hunt
Langley Research Center

SUMMARY

An experimental study of surface pressure distributions on a family of blunt and sharp large angle cones was made in hypersonic flows of helium, air, and tetrafluoromethane. The effective isentropic exponents of these flows were 1.67, 1.40, and 1.12. Thus, the effect of large shock density ratios such as might be encountered during planetary entry because of "real-gas" effects could be studied by comparing results in tetrafluoromethane with those in air and helium. It was found that shock density ratio had a large effect on both shock shape and pressure distribution. The differences in pressure distribution indicate that for atmospheric flight at high speed where "real-gas" effects produce large shock density ratios, large-angle cone vehicles can be expected to experience different trim angles of attack, drag coefficient, and lift-drag ratios than those for ground tests in air wind tunnels. Comparison of the data with several theories indicated that (1) for sharp cones having attached shock waves, the sharp-cone solutions provide a good prediction of pressure, and (2) for both sharp and blunt cones having subsonic flow over the forebody, the semiempirical, $\sin^2$-deficiency method of Love gave the best prediction of pressure distribution.

INTRODUCTION

The use of aerodynamic drag and/or lift as a means for deceleration of a vehicle entering the rarefied atmosphere of Mars requires the use of a high-drag entry configuration. At the present time, cones having total cone angles as high as 140° and practically no afterbody are being considered. At supersonic and hypersonic speeds, the aerodynamic characteristics, including the surface pressure distribution, shock shape, drag, stability, and lift-drag ratio, of such configurations are determined almost exclusively by the forebody flow field. Several previous investigations (refs. 1 to 3) have shown that for hypersonic speeds (free-stream Mach numbers greater than 4), these characteristics primarily depend on the shock density ratio, which, in turn, is dependent on the vehicle speed, and atmospheric composition, pressure, and temperature. Variations in aerodynamic characteristics due to these parameters are the result of real-gas effects, such as dissociation or excitation of higher degrees of freedom of the gas. There is no direct dependence on Mach number. Therefore, the aerodynamic characteristics on blunt vehicles at hypersonic speed can be simulated by matching the shock density ratio. Flight density ratios can be duplicated by using an ideal gas flow having a suitable isentropic exponent (refs. 2 and 4). For Mars entry simulation, isentropic exponent values in the range from 1.09 to 1.3 are required.

The purpose of this paper is to provide measured surface pressure data for several large-angle cones at three values of the isentropic exponent: 1.12, 1.4, and 1.67. These data were obtained in the pilot CF_4 facility at the Langley Research Center, the Langley Mach 8 variable-density hypersonic tunnel, and the Langley 22-inch helium tunnel. A large amount of similar data taken in air at various Mach numbers is given in references 5 to 12.

SYMBOLS

Values are given in both SI and U.S. Customary Units. The measurements and calculations were made in U.S. Customary Units.

C_D	drag coefficient
M_∞	free-stream Mach number
p	local surface pressure
p_o	free-stream stagnation pressure
p_3	stagnation pressure behind normal shock
R_b	base radius
R_n	nose radius
R_∞	free-stream Reynolds number based on diameter

S	surface distance
S_{max}	surface distance to maximum body diameter
T_o	stagnation temperature
u_1	free-stream velocity
V_e	entry velocity
α	angle of attack
γ	ratio of specific heats or isentropic exponent
γ_e	effective ratio of specific heats
θ	cone angle
μ	Mach angle
ρ_1	free-stream density
ρ_2	density behind normal shock

SIMULATION OF REAL-GAS EFFECTS ON BLUNT BODIES

As a blunt body enters a planetary atmosphere at hypersonic speeds, the gas molecules that pass through the bow shock are excited to higher vibrational and chemical energy modes. This excitation increases the degrees of freedom of the gas in the shock layer if it is assumed that equilibrium exists and provided that dissociation is not driven near completion. Since both of these conditions are usually met for blunt-body entry, the γ of the gas in the shock layer is reduced below that of the free stream. A large amount of the energy that would have gone into increasing the static temperature behind the bow shock is thus used in exciting vibration energy levels or dissociating the gas molecules. As additional energy is absorbed by the gas molecules entering the shock layer, the conservation laws and the thermophysics of the gas dictate certain changes in the forebody flow. The static temperature, speed of sound, and velocity in the real-gas shock layer are reduced. The static pressure is increased slightly. The density is increased considerably and the shock-layer thickness is reduced in proportion to this increase.

At supersonic and hypersonic speeds, the aerodynamic characteristics, including the lift, drag, moments, and stability, of blunt (high drag, low fineness ratio) configurations such as those studied in this report are determined almost exclusively by the forebody flow field. Several previous investigations have shown, for example, that the drag of such configurations in a constant-gamma flow (air) is insensitive to Mach number. The data (refs. 7 and 8) presented in figure 1 illustrate this point for the 140° cone. Note that C_D is essentially constant for Mach numbers over 3. Other investigations (refs. 1 to 4) have shown that for very high speeds, such configurations have aerodynamic characteristics that, although essentially independent of Mach number, are strongly dependent on real-gas effects such as excitation of vibrational energy levels or dissociation. These real-gas effects have been shown to correlate as a function of density ratio across the strong bow shock $\left(\rho_2/\rho_1\right)$ for blunt configurations.

The changes in aerodynamic characteristics due to real-gas effects associated with high-speed flight (characterized by large shock density ratios) are primarily the results of changes in surface pressures acting on the forebody. The surface pressures are affected by a change in shock density ratio (real-gas effects) in two ways: first, the level of pressure at the stagnation point is changed, and second, distribution of surface pressure relative to stagnation-point pressure is changed.

The density-ratio effect on the stagnation-point pressure level is easily estimated by considering the flow of a perfect gas about a blunt body. By conserving mass and momentum across a normal shock, considering incompressible flow from the shock to the stagnation point, and neglecting the free-stream static pressure compared with that in the shock layer, the following equation is obtained (ref. 2):

$$\frac{p_3}{\frac{1}{2}\rho_1 u_1^2} = 2 - \frac{1}{\rho_2/\rho_1} \tag{1}$$

This approximate equation which applies for real as well as ideal gases shows that the nondimensional stagnation pressure level on a blunt body is a function only of the shock-density ratio. Doubling the density ratio increases the pressure by about 5 percent.

In order to determine the factors influencing the pressure distribution on blunt bodies, a one-strip integral method was exercised (ref. 2) over a spherical segment, a 120° cone, and a 140° cone at various values of Mach number and γ and thus at various density ratios. The results indicated that the pressure distribution on these bodies depended essentially on the shock density ratio only for Mach numbers of 6 or larger.

These results (ref. 2) are restricted to bodies on which sonic velocities occur at the point of maximum body radius.

One way to simulate inviscid real-gas effects on blunt bodies is to test in a substitute gas flow which provides the correct value of density ratio without any dissociation. The shock density ratio in the substitute gas is a function of both Mach number M_∞ and isentropic exponent γ. For an ideal gas (ref. 13), the expression for the density ratio across a normal shock is

$$\frac{\rho_2}{\rho_1} = \frac{(\gamma + 1)M_\infty{}^2}{(\gamma - 1)M_\infty{}^2 + 2} \tag{2}$$

An effective value of gamma γ_e can be defined as the ideal or substitute gas value which gives the correct normal shock density ratio when the free-stream Mach number in equation (2) is used. The distribution of density ratio with shock angle in flight is such that matching the normal-shock density ratio also insures matching of the oblique-shock density ratio for shock angles above 50°. At large hypersonic Mach numbers, the density ratio becomes a function of gamma only; however, as γ decreases, the Mach number at which this condition is reached increases.

A calculation of γ_e needed to simulate the real-gas effects (shock density ratio) during Mars entry has been made by Allison and Bobbitt (ref. 4). They calculated γ_e from equation (2) for various Mars model atmospheres and different initial entry speeds of a 140° cone on a ballistic trajectory. The results of their calculation for a 4.572 km/sec (15 000 ft/sec) entry into a mean Mars model atmosphere are shown in figure 2. Note that γ_e varies from 1.08 to 1.30 during entry. At maximum dynamic pressure, the value is about 1.14. To account for real-gas effects on the drag coefficient, they used a C_D which was a function only of γ_e (hypersonic condition) as shown in figure 3. The results shown in figure 3 are based on ideal gas calculations for an angle of attack of 0° and on the use of the theoretical calculation procedure of reference 14. The data points presented in this figure (above drag curve) are from the integrated pressure distribution presented in this paper.

At the present time, no methods for calculation of the flow over this configuration at angles of attack for values of γ below 1.2 (ref. 15) are known to the authors. Thus, experimental data obtained at several values of γ_e will enhance the assessment of real-gas effects for such configurations.

APPARATUS AND TEST CONDITIONS

Facilities

Pilot CF_4 facility at the Langley Research Center $\left(\rho_2/\rho_1 \approx 12\right)$.- The pilot CF_4 facility at the Langley Research Center is a small facility which has a contoured axisymmetric nozzle terminating in a 15.24-cm-diameter (6-in.) test section. It has a uniform test-section flow of tetrafluoromethane $\left(CF_4\right)$ at a Mach number of 6.25 and γ_e of 1.12. For these tests, stagnation conditions were approximately 700 K (800° F) and 12.4 MN/m^2 (1800 psig). A complete description of this facility is given in reference 2.

Langley Mach 8 variable-density hypersonic tunnel $\left(\rho_2/\rho_1 \approx 5.6\right)$.- The Langley Mach 8 variable-density hypersonic tunnel is a blowdown facility which has a contoured axisymmetric nozzle with a 45.72-cm-diameter (18-in.) test section. The test medium, air, is heated to 811 K (1000° F) and stagnation pressures range from 0.206 to 20.68 MN/m^2 (30 to 3000 psig). The test-section flow is at a nominal Mach number of 8 and is an ideal gas with a γ of 1.4. This facility is described further in reference 16.

Langley 22-inch helium tunnel $\left(\rho_2/\rho_1 \approx 4\right)$.- The Langley 22-inch helium tunnel uses purified helium as the test gas. A contoured nozzle gives a γ of 1.67, ideal gas flow at a Mach number of 20 in the 57.15-cm-diameter (22.5-in.) test section. The stagnation temperature can be heated to 478 K (400° F) at pressures from 3.45 to 24.82 MN/m^2 (500 to 3600 psig). This facility is also described further in reference 16.

Models and Instrumentation

Sharp and sphere nose conical models with cone angles of 100°, 120°, and 140° were tested. The geometry of the models is illustrated in the following sketch:

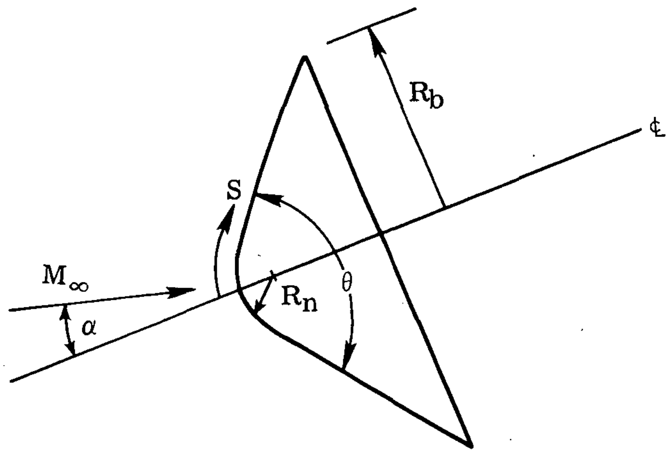

Surface pressure orifices 0.102-cm (0.040-in.) diameter were located along one ray. Data for the windward and leeward rays were obtained by rotating the cones 180°. Photographs of the models and stings are shown in figures 4 and 5.

The blunt models had a nose radius R_n of 0.476 cm (0.1875 in.). For the tests in helium, all the blunt models had a ratio of nose radius to base radius of 0.25. The 1.905-cm (0.75-in.) base radius was too large to run in the small CF_4 tunnel so all models were machined to a base radius of 1.588 cm (0.625 in.). Therefore, the models tested in both CF_4 and air had a ratio of nose radius to base radius of 0.30. The nondimensional locations S/S_{max} of the pressure orifices for the CF_4 and air test therefore differ slightly from those of the helium tests.

For all tests, pressure measurements were made by use of diaphragm type capacitance gages. The gages were adjusted and calibrated before each set of tests and the gage outputs were recorded on magnetic tape by an analog to digital data converter.

Test Conditions

To obtain data at different values of γ, tests were made at hypersonic speeds in air, helium, and tetrafluoromethane and at essentially ideal gas conditions. The following table summarizes the test conditions:

Test condition	CF_4	Air	Helium
M_∞	6.2	7.9	20.3
γ	1.12	1.40	1.67
ρ_2/ρ_1	12.2	5.56	3.97
p_o, MN/m^2 (psia)	9.31 (1350)	1.38 (200)	7.0 (1015)
T_o, K (°F)	700 (800)	700 (800)	305 (90)
R_b, cm (in.)	1.588 (0.625)	1.588 (0.625)	1.905 (0.750)
R_n, cm (in.)	0 and 0.476 (0 and 0.1875)	0 and 0.476 (0 and 0.1875)	0 and 0.476 (0 and 0.1875)
θ, deg	100, 120, 140	100, 120, 140	100, 120, 140
α, deg	0, 10, 20	0, 5, 10, 15	0, 5, 10
$p_3/\frac{1}{2}\rho u^2$	1.99	1.84	1.76
p_3/p_o	0.00126	0.00875	0.00269

RESULTS AND DISCUSSION

Shock Shape

Photographs of the flow about the models were taken by a shadowgraph technique in CF_4 and by schlieren techniques in air and helium. These are shown in figures 6 to 14. Note that in CF_4, the shock appears to be attached to the sharp 120° cone at an angle of attack of 0°, whereas it is detached in both air and helium. Note also the reduction in both shock wave angle and shock standoff distance with decreasing γ, even though the Mach number is increasing.

A comparison of the shock wave angle and shock standoff distance is given in figure 15. This figure is a sketch of the shock shape for all three gases on the 100° sphere-cone at an angle of attack of 10°. The standoff distance at the nose is approximately proportional to the inverse shock density ratio $(\rho_2/\rho_1)^{-1}$. The shock shape comparison several base diameters downstream is of interest. The shock in each gas must eventually approach the limiting angle for an infinitesimally weak wave or Mach angle. This Mach angle is simply

$$\mu = \sin^{-1} \frac{1}{M_{\infty}} \tag{3}$$

and varies greatly for the different test gases because of the Mach number difference. The Mach angles are 9.2°, 7.2°, and 2.8°, respectively, for CF_4, air, and helium. These limiting Mach angles are shown in figure 15 for convenience. Note that in CF_4, the shock wave slope approaches its Mach angle at a distance much closer to the rear of the body than for either air or helium. Extrapolation along the Mach lines shown indicates that the Mach 6.2 CF_4 shock wave would intersect the Mach 20 helium shock wave about 12 base diameters downstream of the rear of the model.

Surface Pressure Distributions

The measured surface pressure distributions are presented in figures 16 to 21. In every case, the measured local pressure has been nondimensionalized by the measured stagnation pressure behind a normal shock at the test condition. The data are shown for the vertical plane of symmetry of the model with results from all three test gases shown on the same plots where possible. The large open symbols indicate data points and the test gas in which data were taken. The small solid symbols are used to indicate the gas for which the various theories apply. Four theories are compared with the data. The well-known Newtonian theory which, of course, is independent of the test gas is shown in every figure; however, the other theories are shown only where they are applicable. For example, the cone solutions of reference 17 apply only to the sharp-cone configurations for angles of attack and test conditions where the shock wave is attached. In figure 16(c), the cone solution is not shown for helium since a 100° cone at an angle of attack of 10° in helium has a detached shock wave.

Sharp cone pressures.- At $\alpha = 0^{\circ}$, all the data for the 100° sharp cone (fig. 16(a)) agree reasonably well with the predictions of the cone solutions except near the sharp corner. For S/S_{max} increasing above 0.6, the helium pressures begin to fall off. This decrease also occurs in air for S/S_{max} larger than 0.8, but is very small or nonexistent in CF_4. The reason for the "fall-off" is because the subsonic surface flow must accelerate to sonic at the sharp corner and since the CF_4 forebody flow is already very near sonic, it requires less acceleration at the corner than does the more subsonic helium and air forebody flows. The value of surface pressure ratio is very strongly dependent on the shock density ratio and thus the value of γ (20 percent higher in helium than in CF_4). The level decreases with an increase in density ratio, the CF_4 data approaching the value predicted by Newtonian theory. Newtonian theory is based on the assumption of an infinite density ratio across the shock (ref. 18), and thus represents the limiting case where $\gamma = 1.0$. At angles of attack, the cone solutions again give the best agreement with the data except for angles of attack where the local deflection angle is very near the shock detachment angle (as happens for air at $\alpha = 10^{\circ}$ on the windward side, fig. 16(c)), or is greater than the shock detachment angle where cone solutions are not applicable. Once the shock wave becomes detached, the $\sin^2$-deficiency method of reference 19 gives the best agreement. By examination of the pressure levels on the windward ray, it appears that the shock wave detaches for an angle of attack of less than 5° in helium, about 10° in air, and near 20° in CF_4.

The data for the 120° sharp cone (fig. 17) show the same general trends as the 100° cone data, except that for $\alpha = 0^{\circ}$ only the CF_4 data indicate an attached shock. Comparison of the distributions for the three values of γ at $\alpha = 10^{\circ}$ (fig. 17(c)) indicates large differences in pressure level, particularly on the leeward ray. These different pressure levels would be expected to result in different trim angles of attack, drag, and lift-drag ratio in the different γ flows. Thus, one would expect that for this configuration in high-speed flight where real-gas effects increase the shock density ratio and thus lower the effective gamma of the flow, there would be accompanying changes in trim, drag, and lift-drag ratio.

For the 140° cone at $\alpha = 0^{\circ}$ (fig. 18(a)), the shock wave is detached for all three gases. This set of data allows a good comparison of the one-strip integral theory of reference 14 with the $\sin^2$-deficiency method of reference 19. Both of these methods require that the sonic point be located at the point of maximum body diameter. The data shown for positive and negative surface distances are identical and, for clarity, the method of reference 19 is compared with the data for -S and the theory of reference 14 is compared with the data for +S. The semiempirical method of reference 19 provides much better agreement with the data. At other angles of attack, the data and theory show trends similar to those for the smaller angle cones.

Blunt cone pressures.- Data for the 100° blunt cone are shown in figure 19. For $\alpha = 0^{\circ}$, the pressure level on the conical portion $\left(S/S_{max} > 0.16\right)$ shows the same strong dependence on γ and about the same pressure level as the sharp 100° cone data. The pressure-ratio values for helium and air both decrease for S/S_{max} greater than 0.6, but the CF_4 data show an increasing pressure in this region. At angles of attack, the pressure level on the conical portion indicates much the same trend as for the sharp cone. Newtonian theory and the method of reference 19 are the only methods of those considered herein which are applicable for the 100° blunt cone, and the method of reference 19 was only applicable to the windward ray at angles of attack where the equivalent blunt cone was entirely subsonic. In all cases, the method of reference 19 gave better agreement with the data. In the vicinity of the spherical nose $\left(-0.16 < S/S_{max} < 0.16\right)$, only three pressure orifices could be located on these small models; one at the point of symmetry, and the other two near the sphere-cone tangency point. Therefore, very little was learned about the detailed pressure distribution on the nose for any of these tests; however, it appears that neither theory gives adequate predictions in this region.

The location of the sonic point on the 120° blunt cone was the point of maximum body diameter for both helium and air at $\alpha = 0^{\circ}$. Thus, both the methods of references 14 and 19 can be compared with the data (fig. 20(a)). Here again, the method of reference 19 gave better agreement. In all cases, the pressure distributions for the three different gases are closer for the 140° cone (fig. 21) than for the smaller angle cones. At $\alpha = 0^{\circ}$ (fig. 21(a)), the flow over the forebody is subsonic for all three gases. Here too, the method of reference 19 provides a better prediction than the method of reference 14 does. At $\alpha = 10^{\circ}$ (fig. 21(c)), a comparison of the data for the three different values of γ indicates significant differences which would be expected to affect trim angle of attack and lift-drag ratio.

CONCLUDING REMARKS

An experimental study of surface pressure distributions on a family of blunt and sharp large-angle cones was made in hypersonic flows of helium, air, and tetrafluoromethane. The effective isentropic exponents of these flows were 1.67, 1.40, and 1.12. Thus, the effect of large shock density ratios such as might be encountered during planetary entry because of "real-gas" effects could be studied by comparing results in tetrafluoromethane with those in air and helium. It was found that shock density ratio had a large effect on both shock shape and pressure distribution. The differences in pressure distribution indicate that for atmospheric flight at high speed where "real-gas" effects produce large shock density ratios, large-angle cone vehicles can be expected to experience different trim angles of attack, drag coefficient, and lift-drag ratios than those for ground tests in air wind tunnels. Comparison of the data with several theories indicated that (1) for sharp cones having attached shock waves, the sharp-cone solutions provide a good prediction of pressure, and (2) for both sharp and blunt cones having subsonic flow over the forebody, the semiempirical, $\sin^2$-deficiency method of Love gave the best prediction of pressure distribution.

Langley Research Center,
National Aeronautics and Space Administration,
Hampton, Va., October 16, 1973.

REFERENCES

1. Anon.: Comparative Studies of Conceptual Design and Qualification Procedures for a Mars Probe/Lander. Volume V: Subsystem and Technical Analyses – Book 2: Aeromechanics and Thermal Control. AVSSD-0006-66-RR (Contract NAS 1-5224), AVCO Corp., May 11, 1966. (Available as NASA CR-66136.)

2. Jones, Robert A.; and Hunt, James L. (With appendix A by James L. Hunt, Kathryn A. Smith, and Robert B. Reynolds, and appendix B by James L. Hunt and Lillian R. Boney): Use of Tetrafluoromethane To Simulate Real-Gas Effects on the Hypersonic Aerodynamics of Blunt Vehicles. NASA TR R-312, 1969.

3. Krumins, Maigonis V.: Drag and Stability of Various Mars Entry Configurations. IAF Paper RE 138, Oct. 1968.

4. Allison, Dennis O.; and Bobbitt, Percy J.: Real-Gas Effects on the Drag and Trajectories of a Nonlifting 140° Conical Aeroshell During Mars Entry. NASA TN D-6240, 1971.

5. Stewart, David A.; and Inouye, Mamoru: Shock Shapes and Pressure Distributions for Large-Angle Pointed Cones in Helium at Mach Numbers of 8 and 20. NASA TN D-5343, 1969.

6. Stallings, Robert L., Jr.; and Tudor, Dorothy H.: Experimental Pressure Distributions on a 120° Cone at Mach Numbers From 2.96 to 4.63 and Angles of Attack From 0° to 20°. NASA TN D-5054, 1969.

7. Walker, Billy; and Weaver, Robert W.: Static Aerodynamic Characteristics of Blunted Cones in Mach-Number Range From 2.2 to 9.5. Tech. Rep. 32-1213 (Contract No. NAS 7-100), Jet Propulsion Lab., California Inst. Technol., Dec. 1, 1967.

8. Campbell, James F.: Supersonic Aerodynamic Characteristics and Shock Standoff Distances for Large-Angle Cones With and Without Cylindrical Afterbodies. NASA TN D-5334, 1969.

9. Campbell, James F.; and Howell, Dorothy T.: Supersonic Aerodynamics of Large-Angle Cones. NASA TN D-4719, 1968.

10. Kurtz, Donald W.: Detailed Pressure Distribution on a Blunted 60-deg Half-Angle Cone at Mach Numbers of 6.08 and 9.46. Tech. Mem. 33-404 (Contract No. NAS 7-100), Jet Propulsion Lab., California Inst. Technol., Sept. 1, 1968.

11. Campbell, James F.: Longitudinal Aerodynamic Characteristics of Several High-Drag Bodies at Mach Numbers From 1.50 to 4.63. NASA TN D-3915, 1967.

12. Gibson, Frederick W.: Aerodynamic Investigation of Some High-Drag Entry Shapes at Mach 15.4. NASA TN D-4134, 1967.

13. Ames Research Staff: Equations, Tables, and Charts for Compressible Flow. NACA Rep. 1135, 1952. (Supersedes NACA TN 1428.)

14. South, Jerry C., Jr.: Calculation of Axisymmetric Supersonic Flow Past Blunt Bodies With Sonic Corners, Including a Program Description and Listing. NASA TN D-4563, 1968.

15. Barnwell, Richard W.: A Time-Dependent Method for Calculating Supersonic Angle-of-Attack Flow About Axisymmetric Blunt Bodies With Sharp Shoulders and Smooth Nonaxisymmetric Blunt Bodies. NASA TN D-6283, 1971.

16. Schaefer, William T., Jr.: Characteristics of Major Active Wind Tunnels at the Langley Research Center. NASA TM X-1130, 1965.

17. South, Jerry C., Jr.; and Klunker, E. B.: Methods for Calculating Nonlinear Conical Flows. Analytic Methods in Aircraft Aerodynamics, NASA SP-228, 1970, pp. 131-155; Discussion, pp. 156-158.

18. Hayes, Wallace D.; and Probstein, Ronald F.: Hypersonic Flow Theory. Academic Press, Inc., 1959.

19. Love, E. S.; Woods, W. C.; Rainey, R. W.; and Ashby, G. C., Jr.: Some Topics in Hypersonic Body Shaping. AIAA Paper No. 69-181, Jan. 1969.

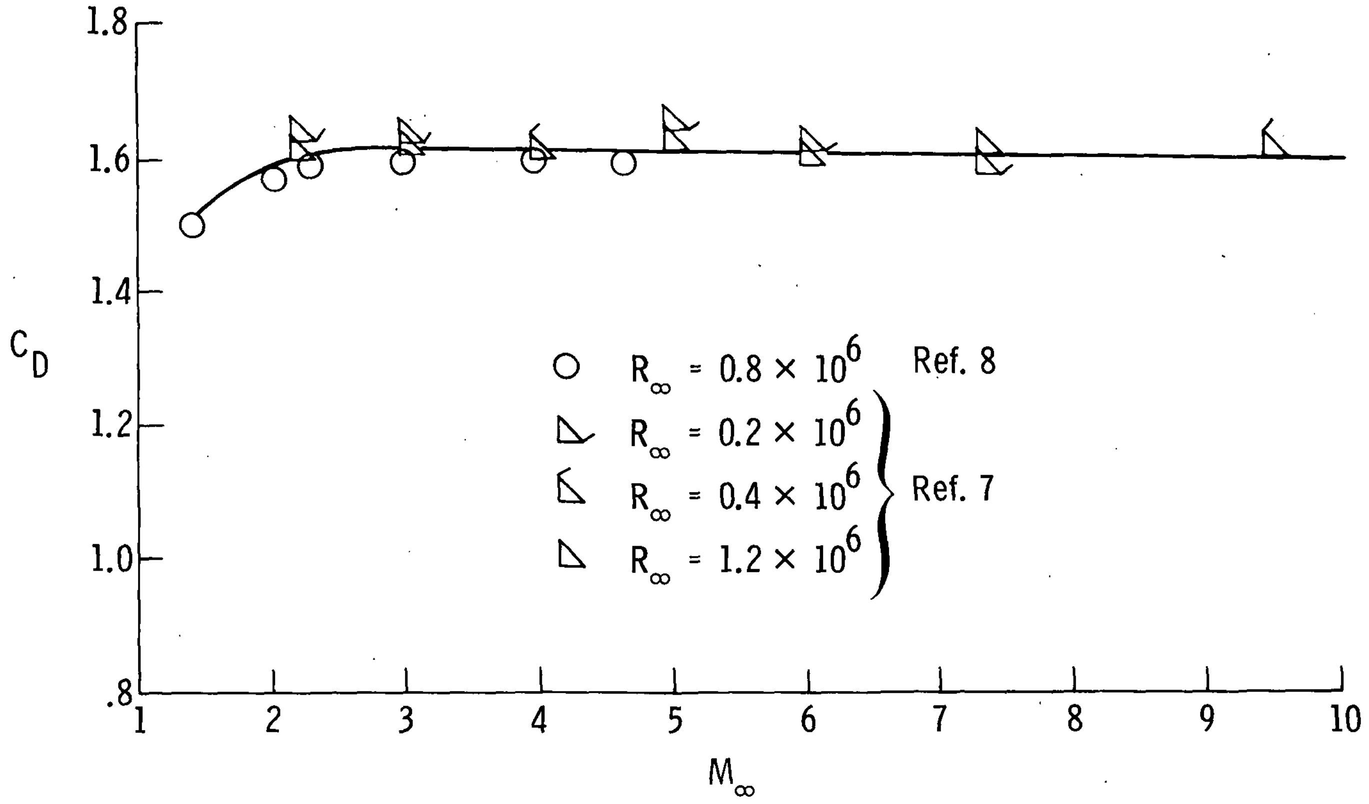

Figure 1.- Variation of measured drag coefficient with Mach number for a 140° cone in air. $\gamma = 1.40$.

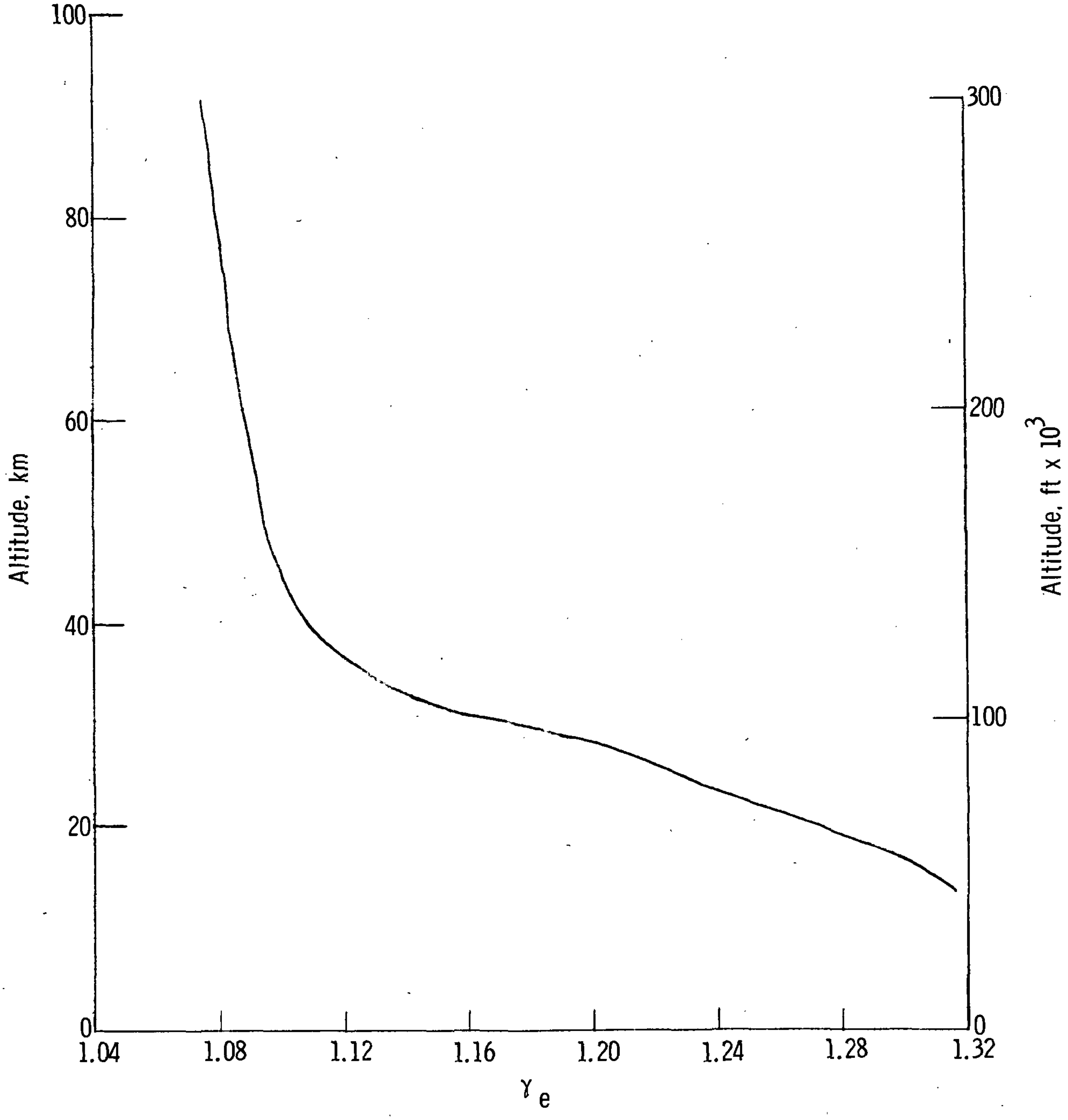

Figure 2.- Variation of γ_e with altitude for 15° flight-path entry into mean Mars atmosphere. V_e = 4.57 km/sec (15 000 ft/sec).

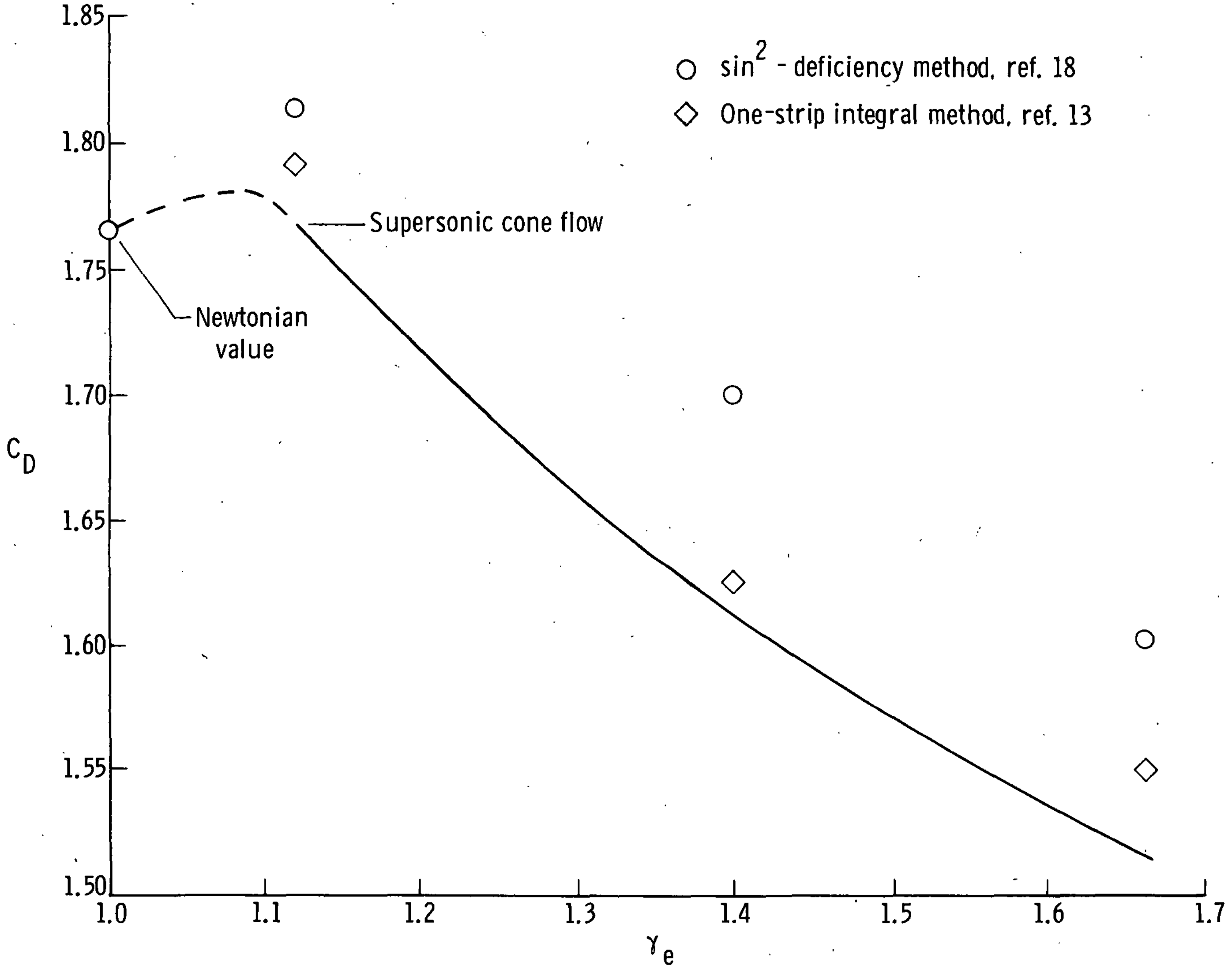

Figure 3.- Variation of drag coefficient for 140° cone with γ_e (taken from ref. 4).

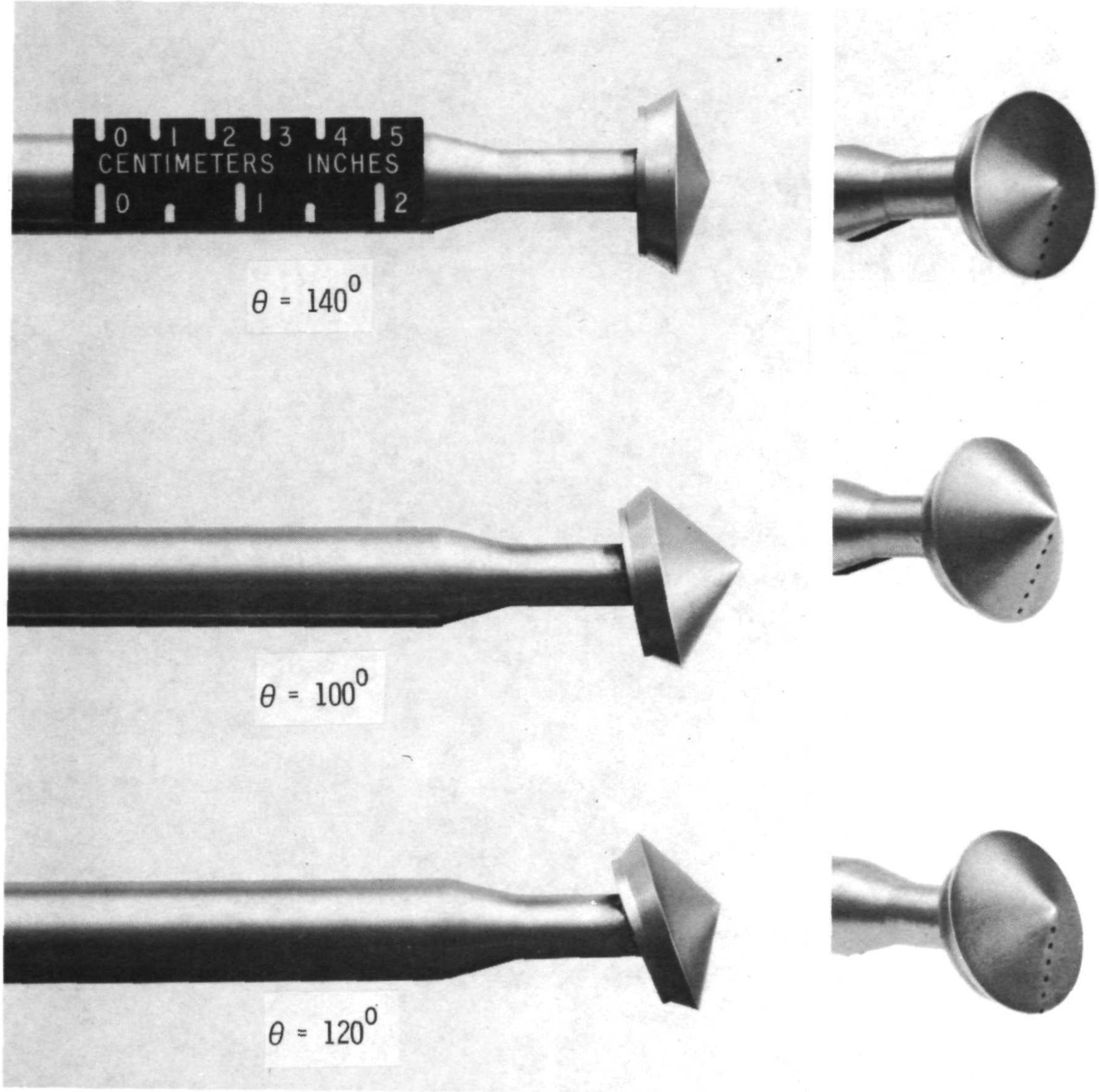

L-73-6899

Figure 4.- Sharp-cone models.

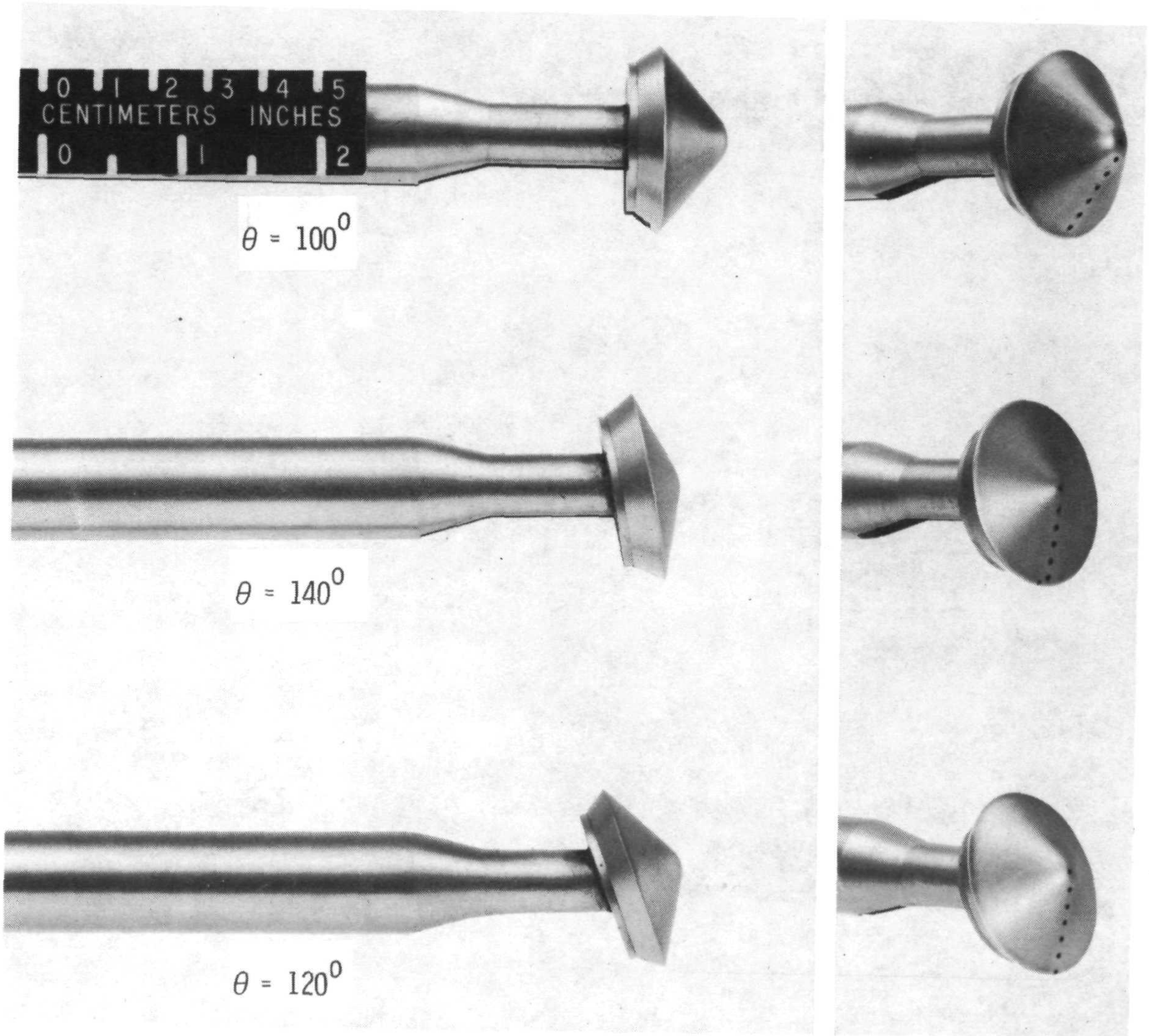

Figure 5.- Sphere-cone models.

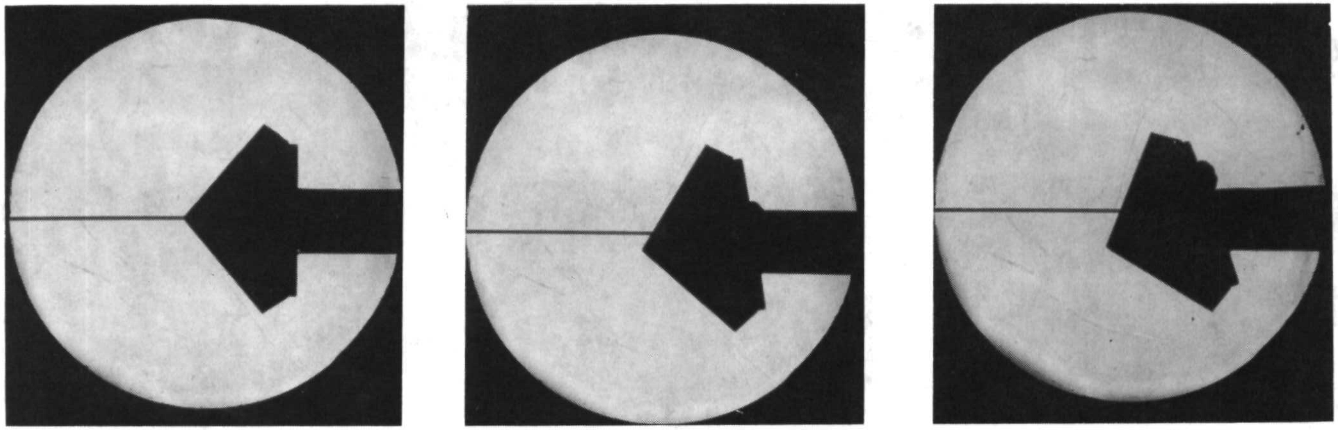

$\alpha = 0^{\circ}$ $\alpha = 10^{\circ}$ $\alpha = 20^{\circ}$

(a) $R_n/R_b = 0$.

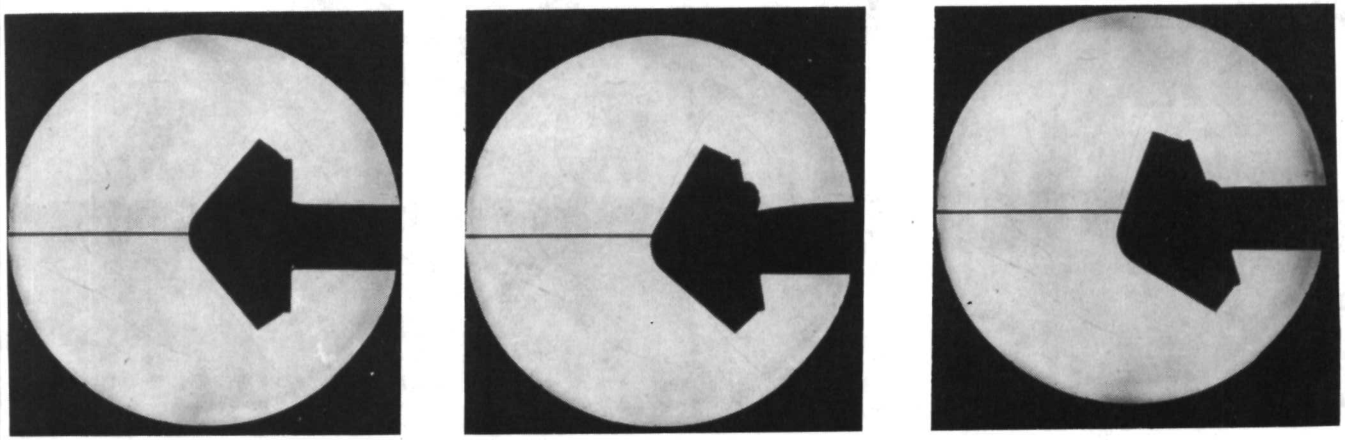

$\alpha = 0^{\circ}$ $\alpha = 10^{\circ}$ $\alpha = 20^{\circ}$

(b) $R_n/R_b = 0.30$.

L-73-8001

Figure 6.- Shadowgraphs of 100° cone in CF_4. $M_{\infty} = 6.25$; $\rho_2/\rho_1 = 12.2$.

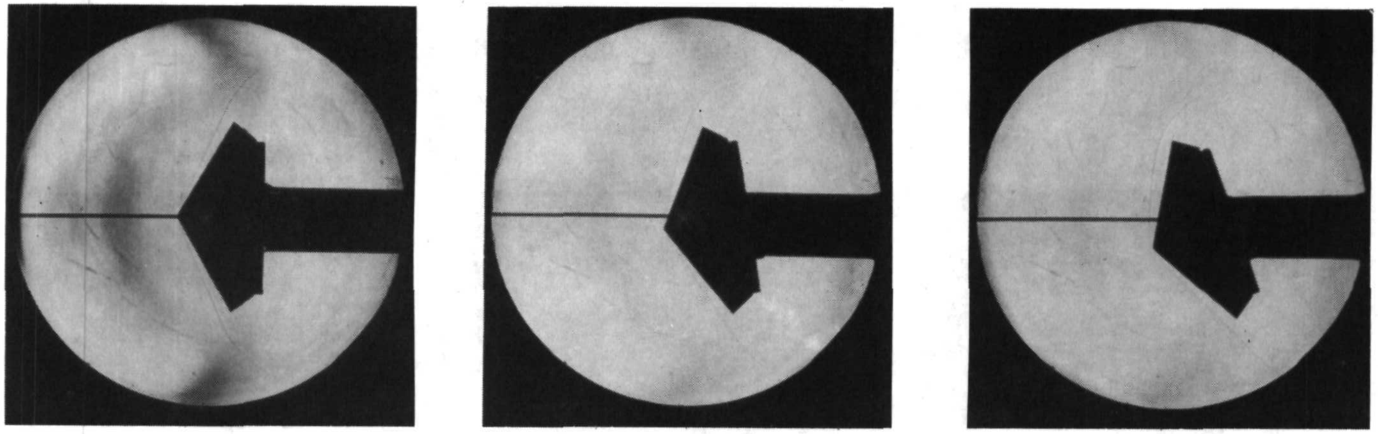

$\alpha = 0^{\circ}$ $\alpha = 10^{\circ}$ $\alpha = 20^{\circ}$

(a) $R_n/R_b = 0$.

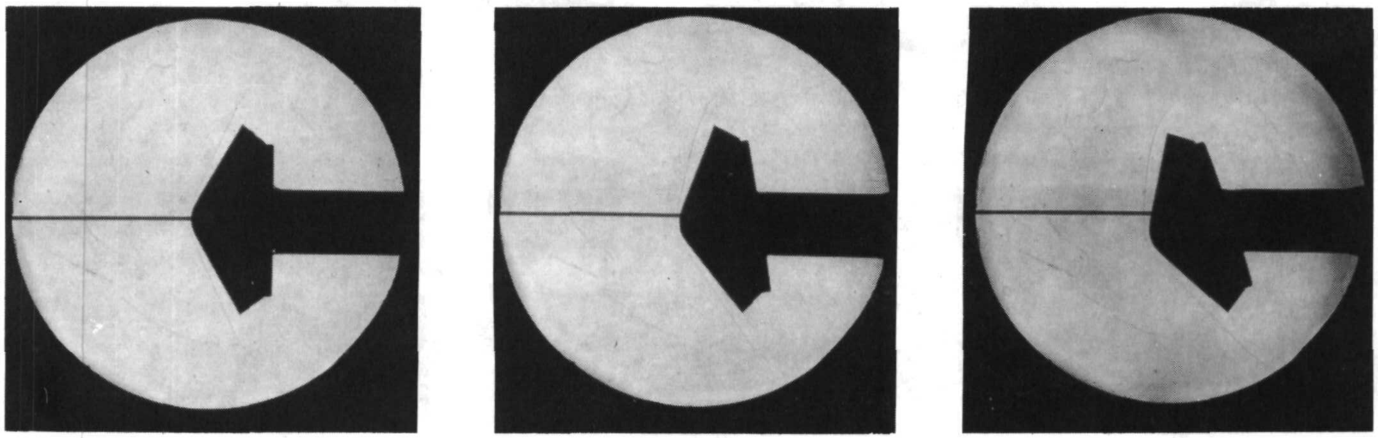

$\alpha = 0^{\circ}$ $\alpha = 10^{\circ}$ $\alpha = 20^{\circ}$

(b) $R_n/R_b = 0.30$.

L-73-8002

Figure 7.- Shadowgraphs of 120° cone in CF_4. $M_\infty = 6.25$; $\rho_2/\rho_1 = 12.2$.

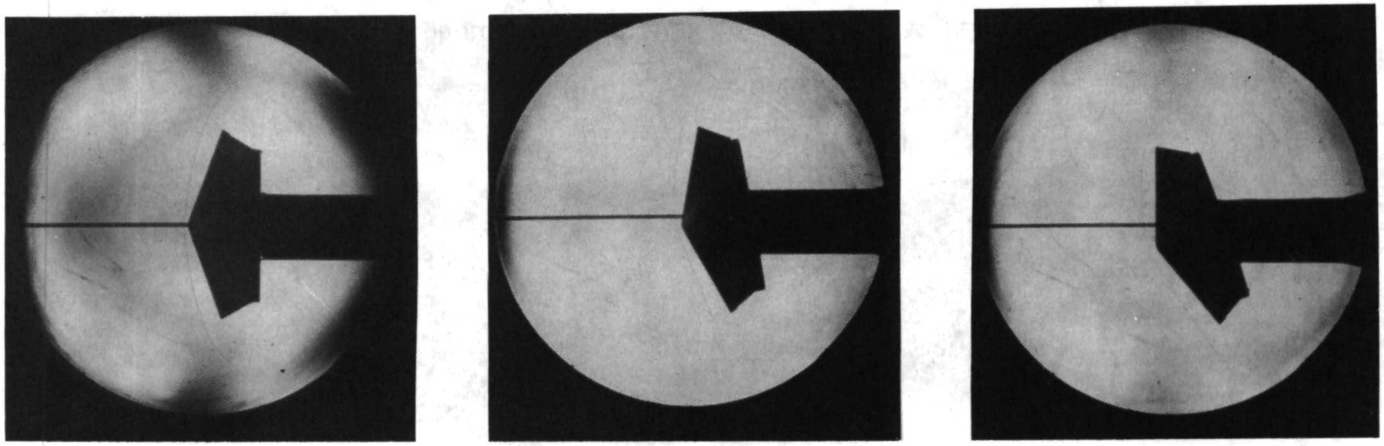

$\alpha = 0^{\circ}$ $\alpha = 10^{\circ}$ $\alpha = 20^{\circ}$

(a) $R_n/R_b = 0$.

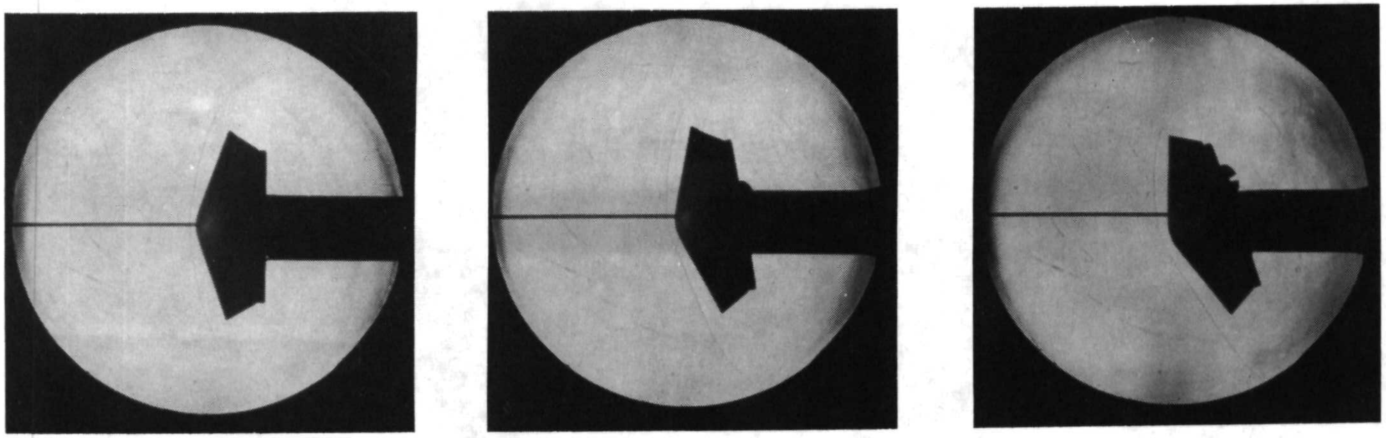

$\alpha = 0^{\circ}$ $\alpha = 10^{\circ}$ $\alpha = 20^{\circ}$

(b) $R_n/R_b = 0.30$.

L-73-8003

Figure 8.- Shadowgraphs of 140° cone in CF_4. $M_{\infty} = 6.25$; $\rho_2/\rho_1 = 12.2$.

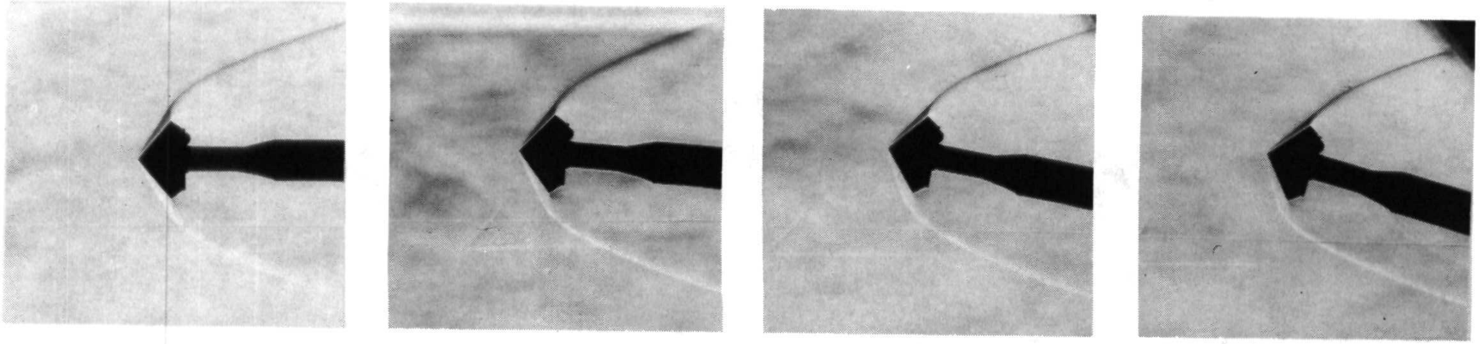

$\alpha = 0^{\circ}$ $\alpha = 5^{\circ}$ $\alpha = 10^{\circ}$ $\alpha = 15^{\circ}$

(a) $R_n/R_b = 0.$

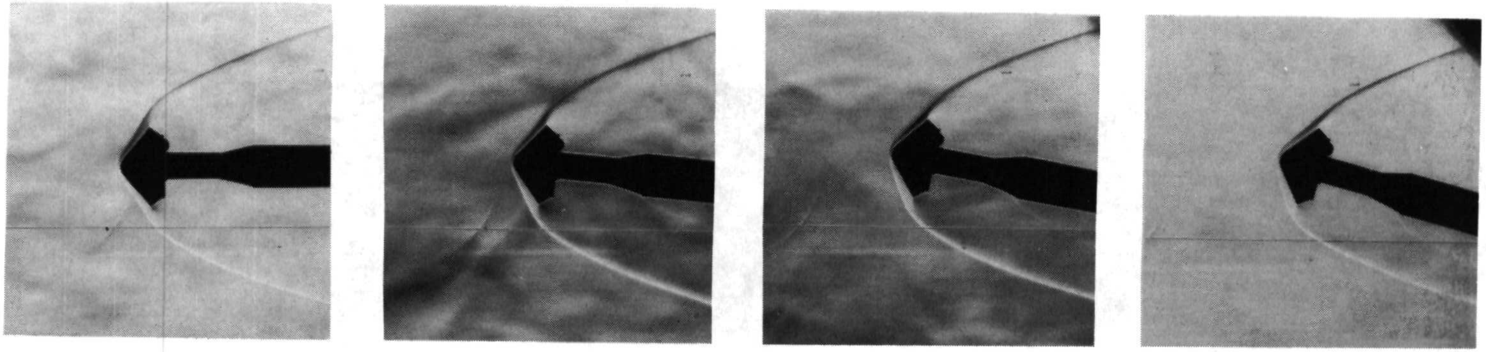

$\alpha = 0^{\circ}$ $\alpha = 5^{\circ}$ $\alpha = 10^{\circ}$ $\alpha = 15^{\circ}$

(b) $R_n/R_b = 0.30.$

L-73-8004

Figure 9.- Schlieren photographs of 100° cone in air. $M_{\infty} = 7.9$; $\rho_2/\rho_1 = 5.6$.

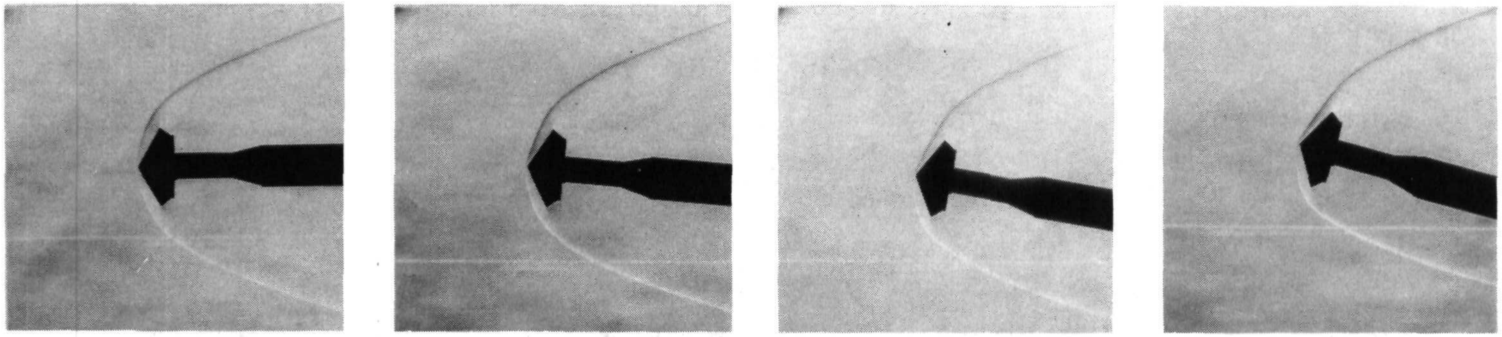

$\alpha = 0^\circ$ $\alpha = 5^\circ$ $\alpha = 10^\circ$ $\alpha = 15^\circ$

(a) $R_n/R_b = 0$.

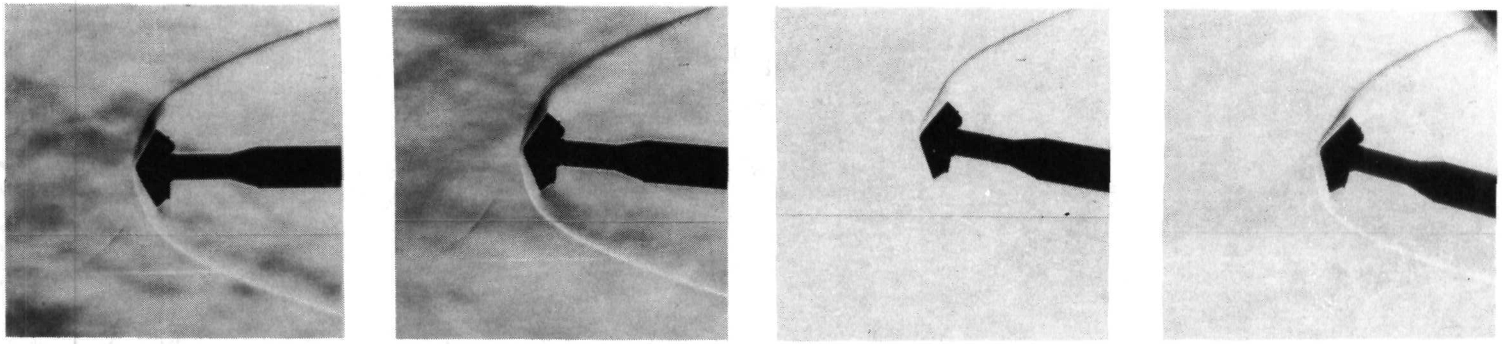

$\alpha = 0^\circ$ $\alpha = 5^\circ$ $\alpha = 10^\circ$ $\alpha = 15^\circ$

(b) $R_n/R_b = 0.30$.

L-73-8005

Figure 10.- Schlieren photographs of 120° cone in air. $M_\infty = 7.9$; $\rho_2/\rho_1 = 5.6$.

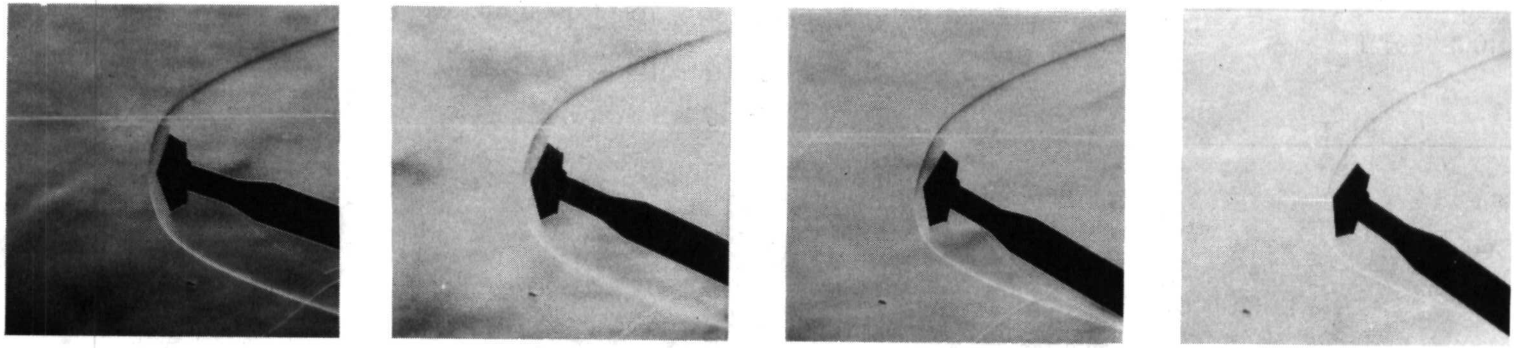

α = 0° α = 5° α = 10° α = 15°

(a) $R_n/R_b = 0$.

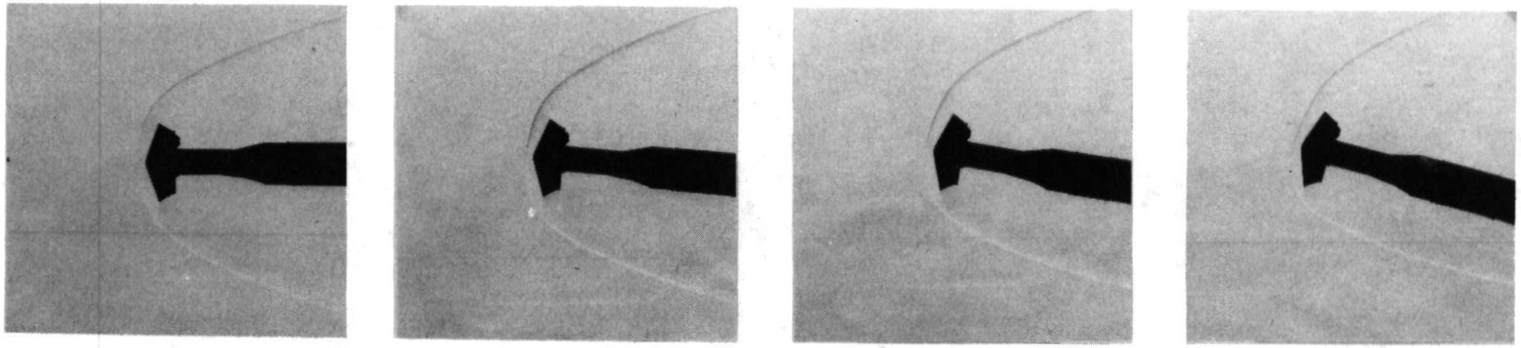

α = 0° α = 5° α = 10° α = 15°

(b) $R_n/R_b = 0.30$.

L-73-8006

Figure 11.- Schlieren photographs of 140° cone in air. $M_\infty = 7.9$; $\rho_2/\rho_1 = 5.6$.

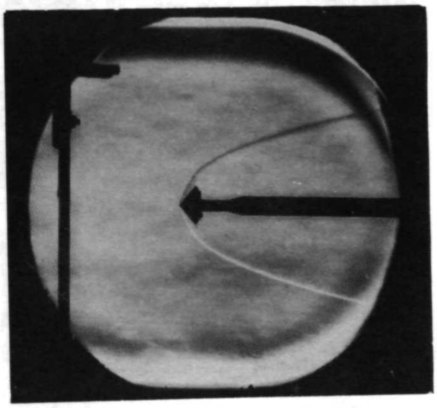

$\alpha = 0^{\circ}$

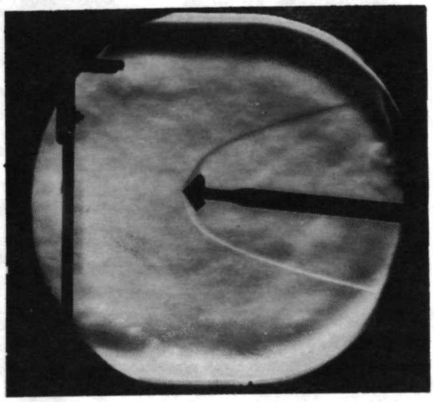

$\alpha = 5^{\circ}$

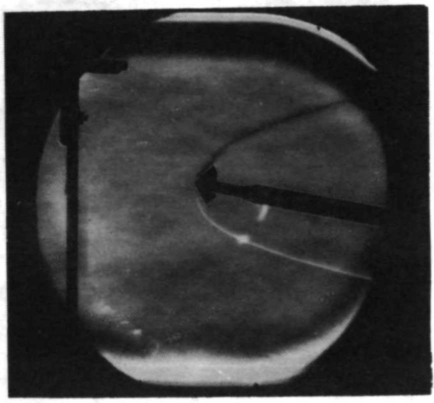

$\alpha = 10^{\circ}$

(a) Sharp cone; $R_n/R_b = 0.25$.

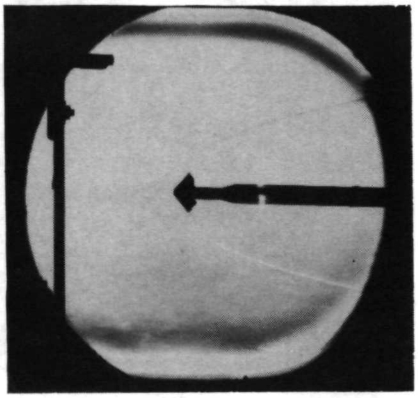

$\alpha = 0^{\circ}$

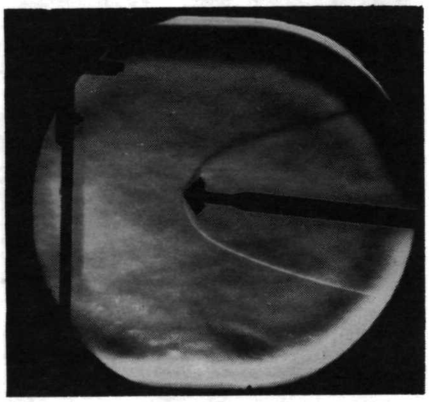

$\alpha = 5^{\circ}$

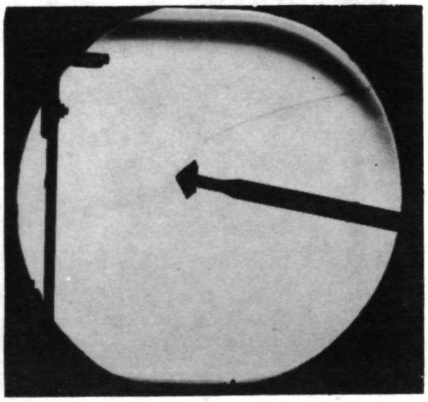

$\alpha = 10^{\circ}$

(b) Blunt cone; $R_n/R_b = 0.25$.

L-73-8007

Figure 12.- Schlieren photographs of 100° cone in helium. $M_\infty = 20.3$; $\rho_2/\rho_1 = 3.97$.

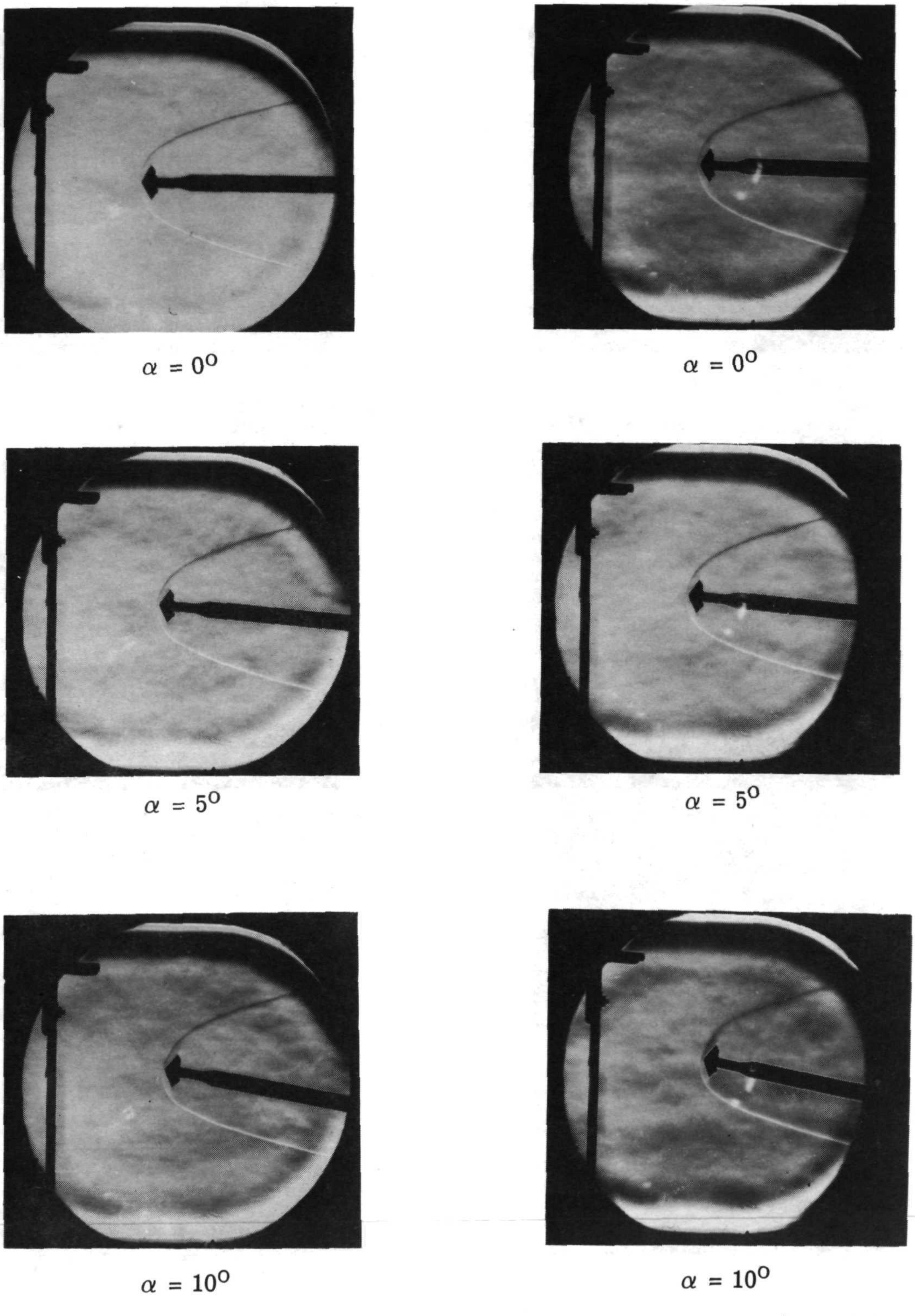

$\alpha = 0^\circ$ $\alpha = 0^\circ$

$\alpha = 5^\circ$ $\alpha = 5^\circ$

$\alpha = 10^\circ$ $\alpha = 10^\circ$

(a) Sharp cone; $R_n/R_b = 0.25$. (b) Blunt cone; $R_n/R_b = 0.25$.

L-73-8008

Figure 13.- Schlieren photographs of 120° cone in helium. $M_\infty = 20.3$; $\rho_2/\rho_1 = 3.97$.

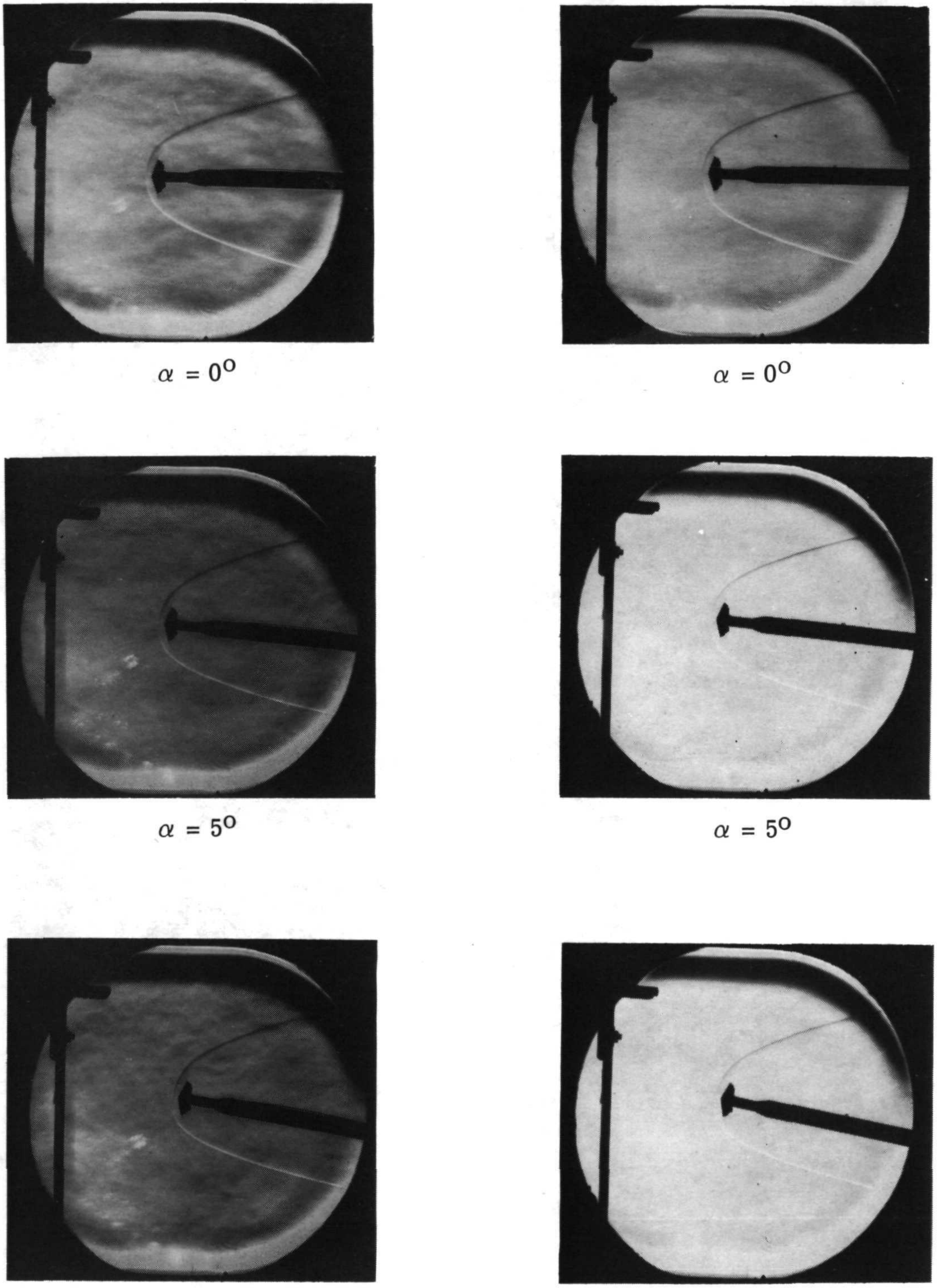

$\alpha = 0^\circ$ $\alpha = 0^\circ$

$\alpha = 5^\circ$ $\alpha = 5^\circ$

$\alpha = 10^\circ$ $\alpha = 10^\circ$

(a) Sharp cone; $R_n/R_b = 0.25$. (b) Blunt cone; $R_n/R_b = 0.25$.

L-73-8009

Figure 14.- Schlieren photographs of 140° cone in helium. $M_\infty = 20.3$; $\rho_2/\rho_1 = 3.97$.

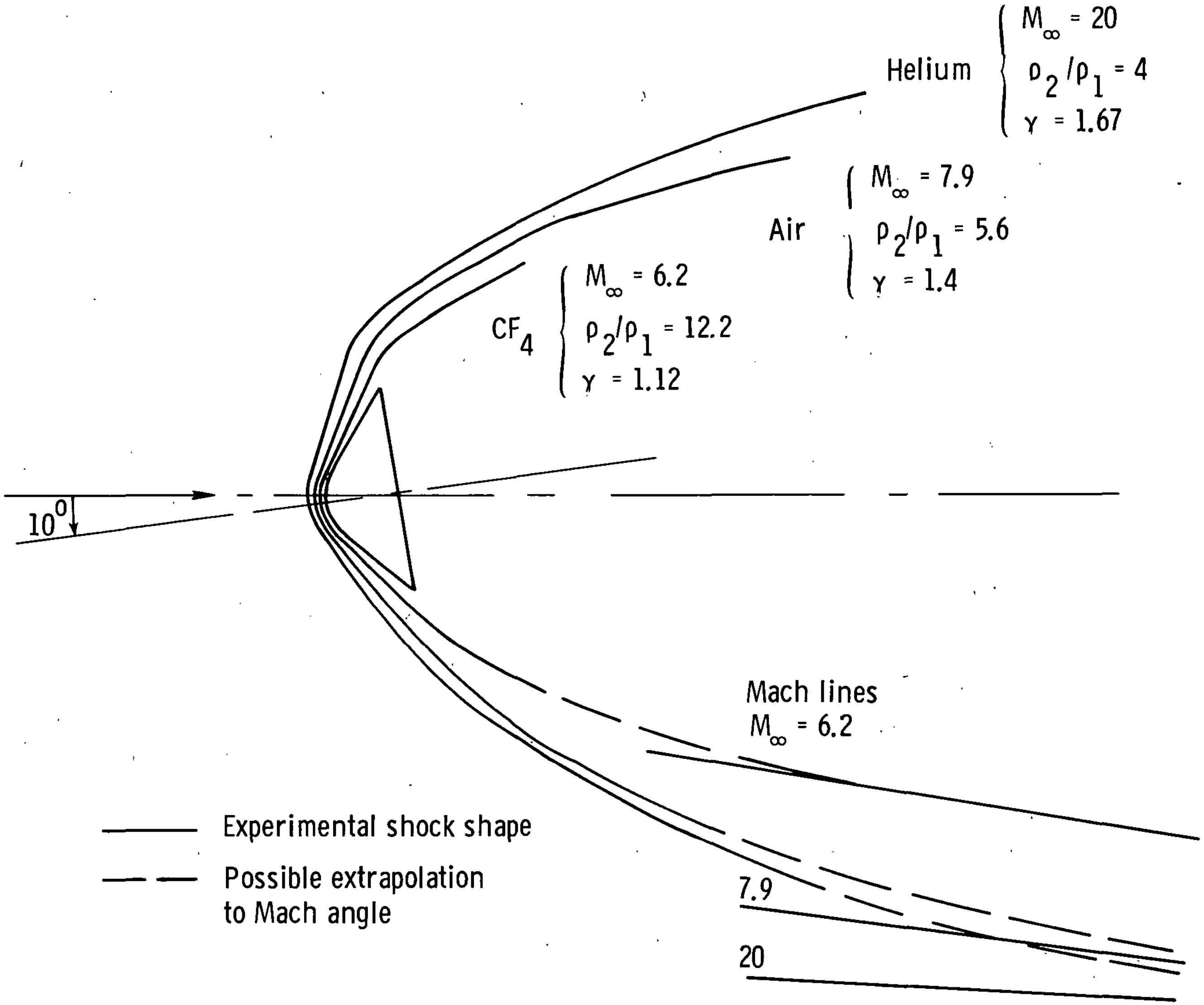

Figure 15.- Shock shape comparison. 100° sphere-cone.

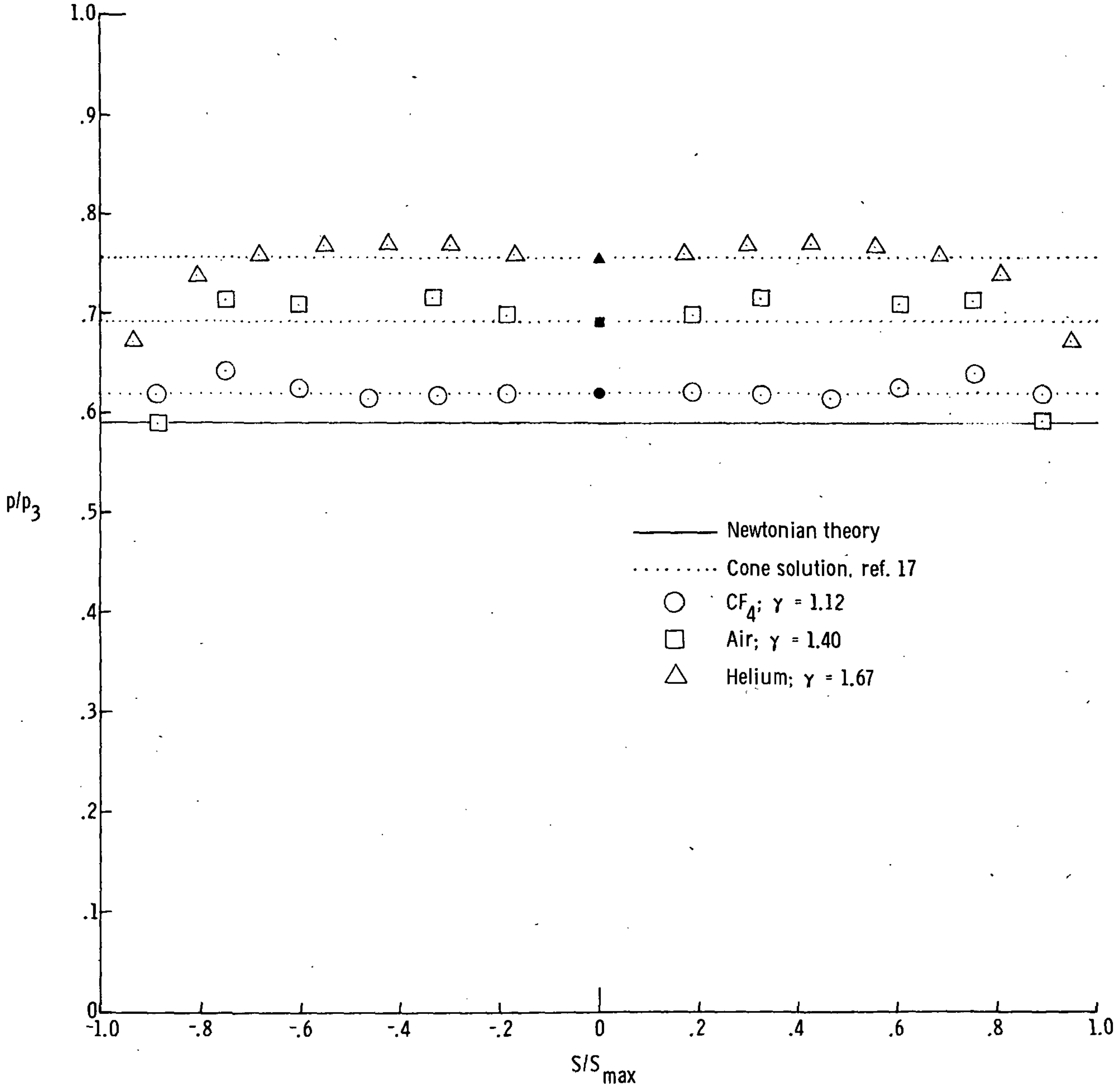

(a) $\alpha = 0^o$.

Figure 16.- Pressure distribution on 100° sharp cone.

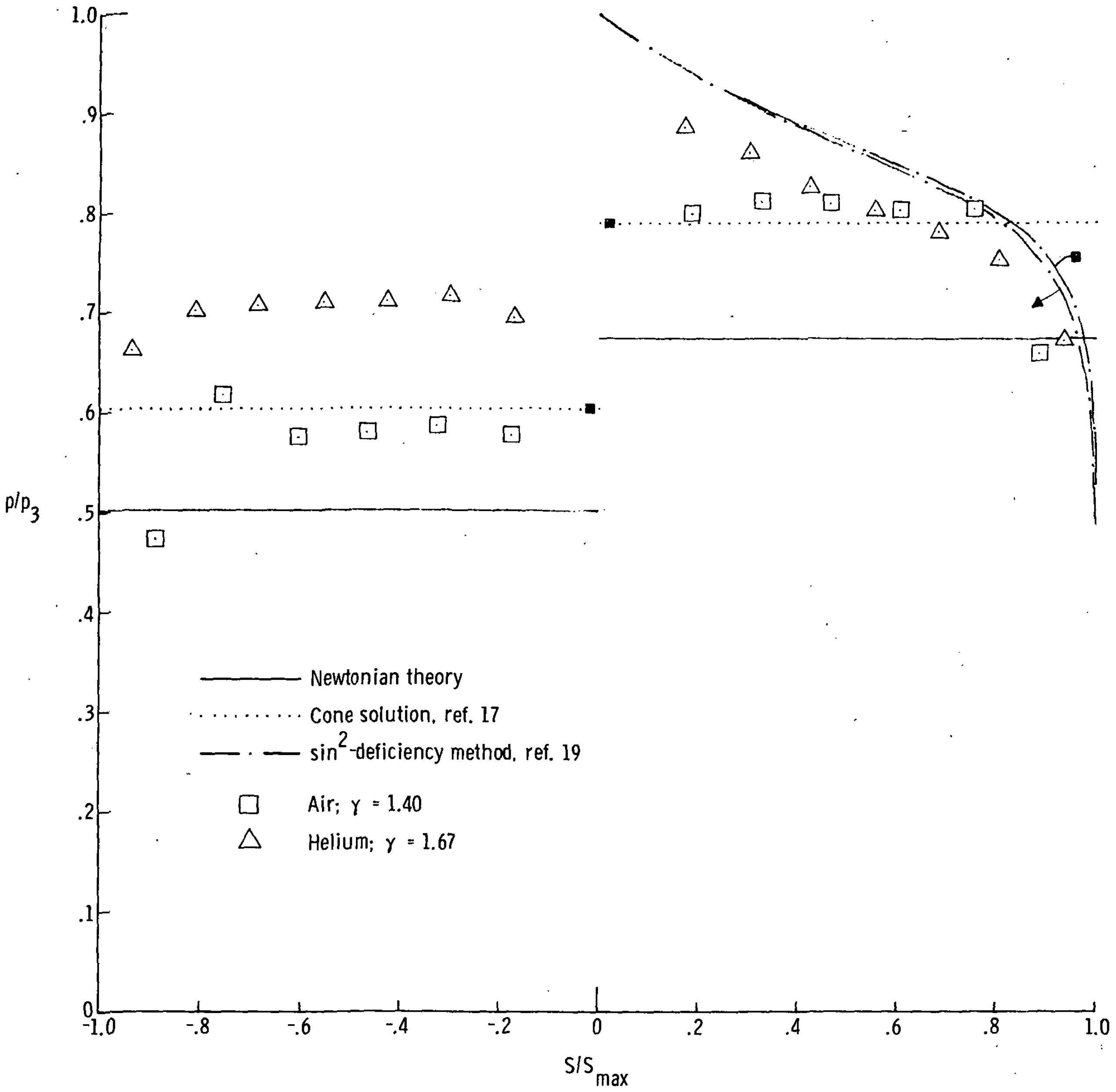

(b) $\alpha = 5^{\circ}$.

Figure 16.- Continued.

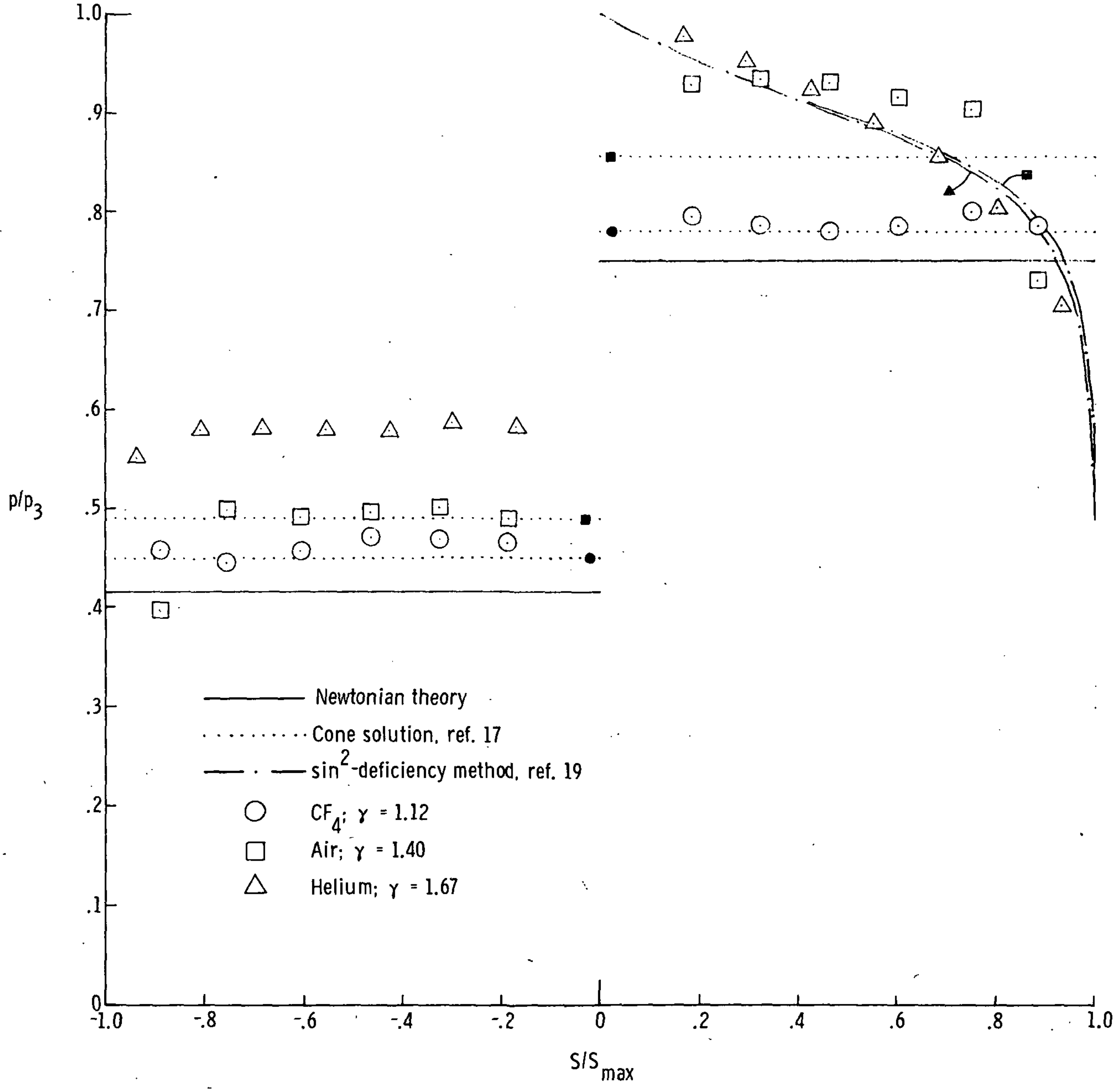

(c) $\alpha = 10^{\circ}$.

Figure 16.- Continued.

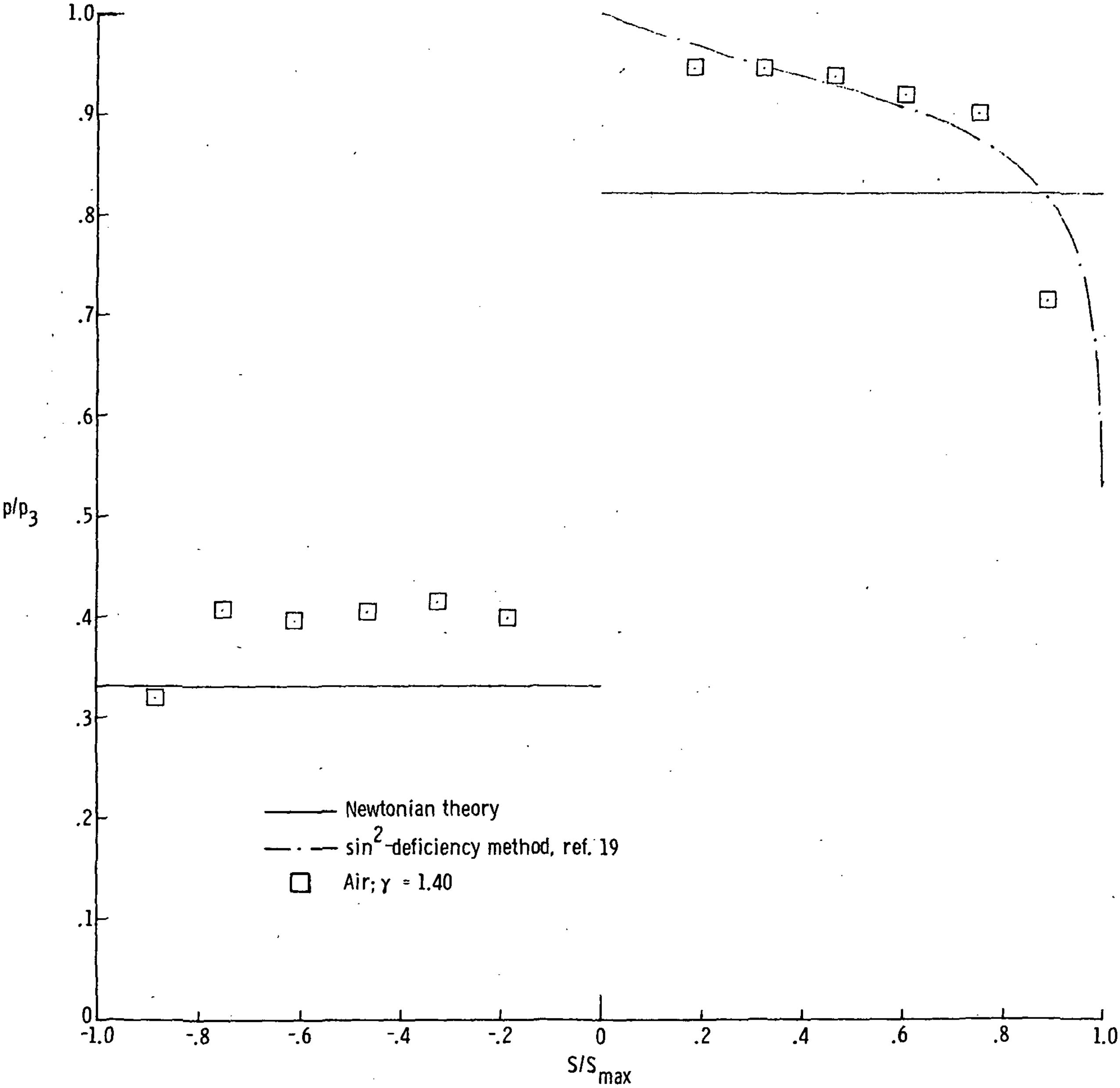

(d) $\alpha = 15^{\circ}$.

Figure 16.- Continued.

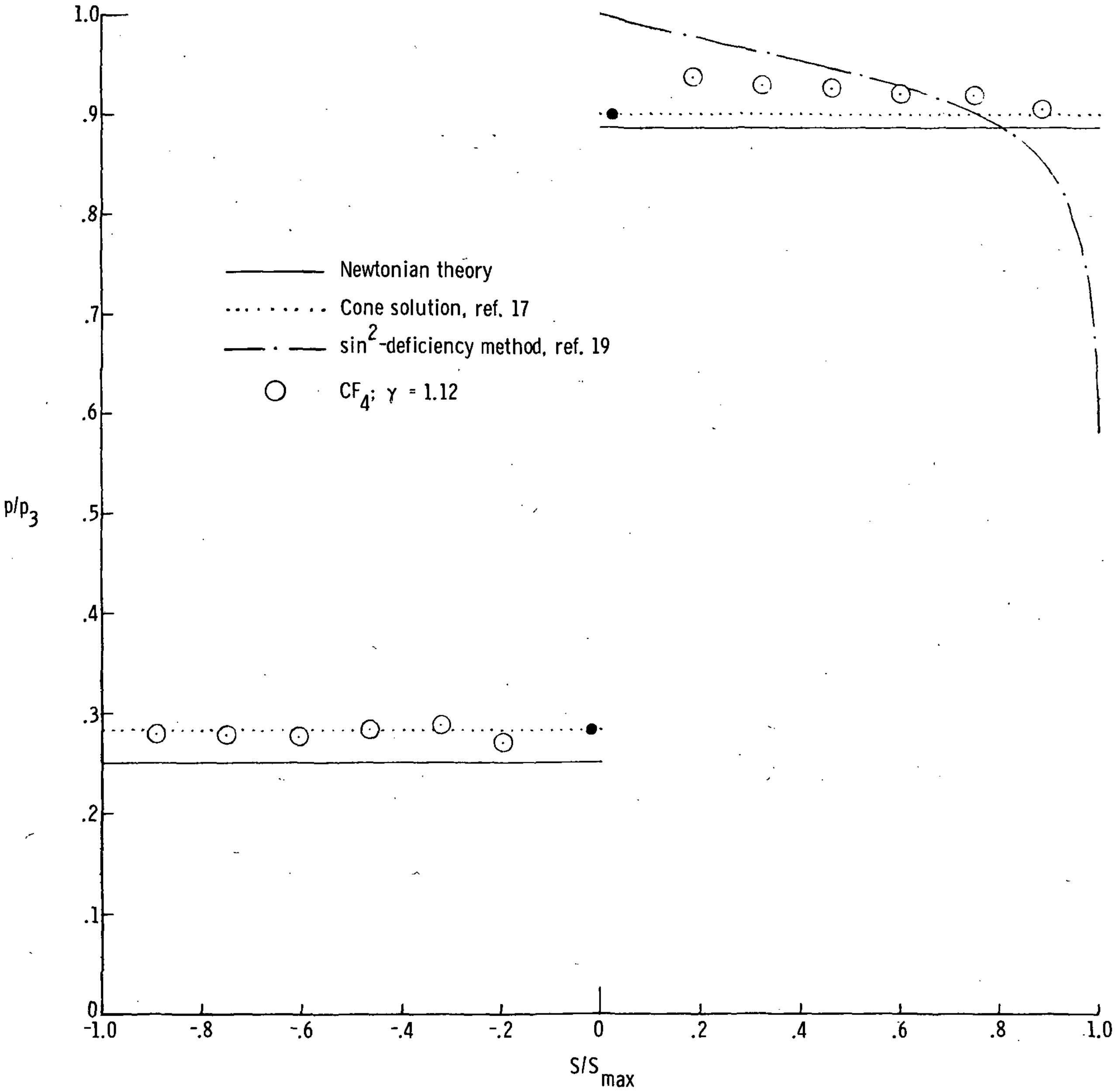

(e) $\alpha = 20^\circ$.

Figure 16.- Concluded.

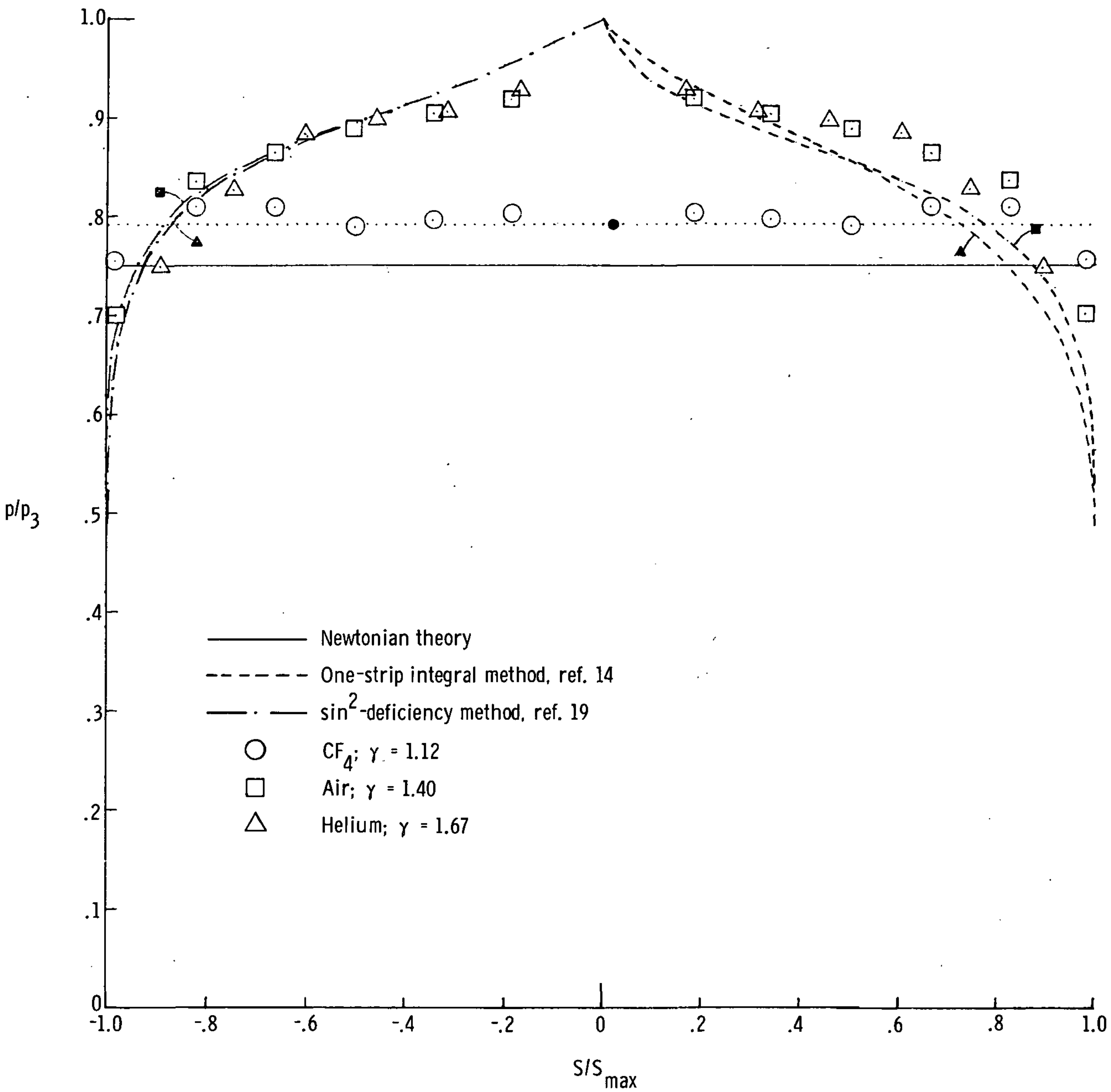

(a) $\alpha = 0^{\circ}$.

Figure 17.- Pressure distribution on 120° sharp cone.

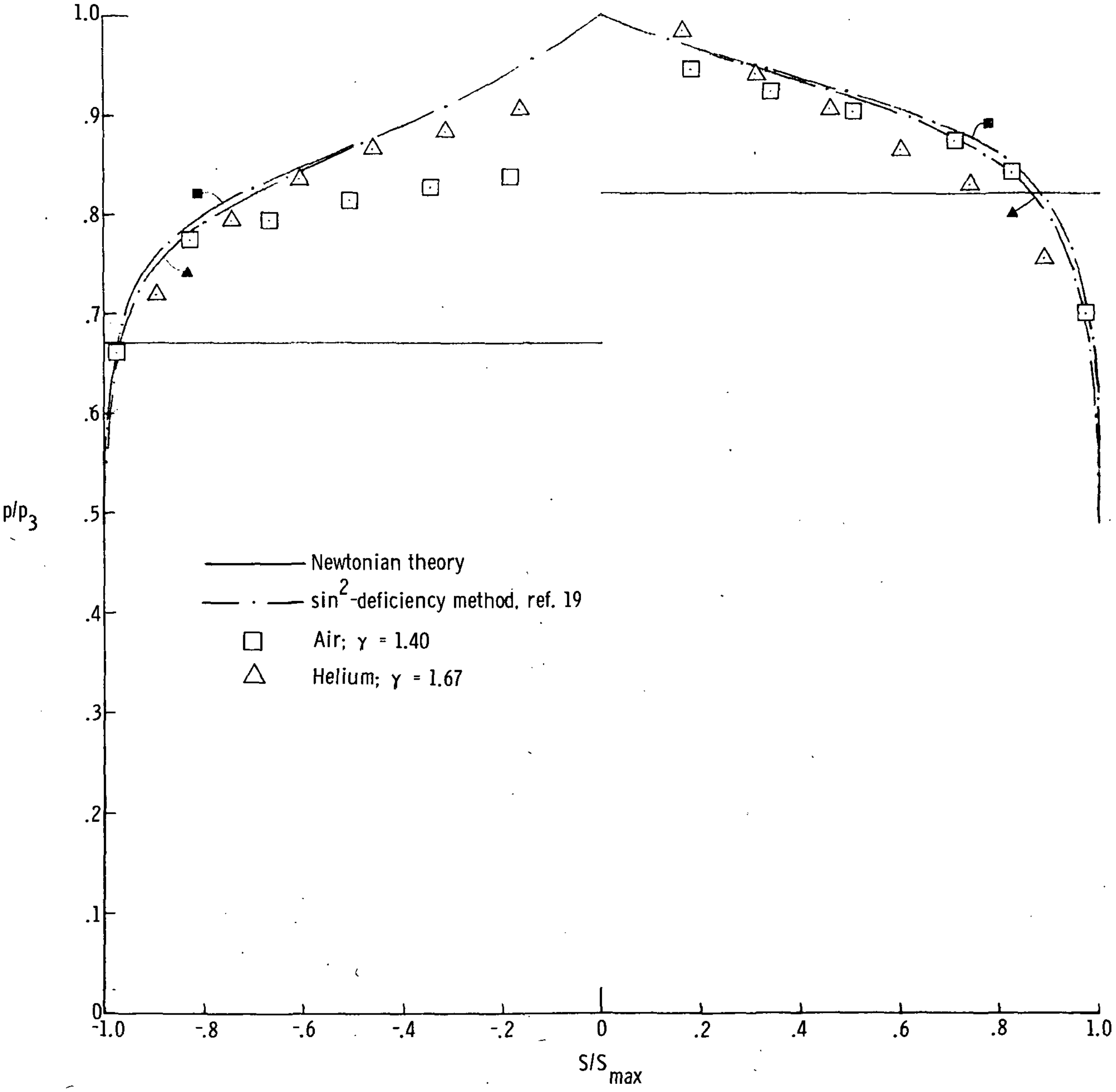

(b) $\alpha = 5^\circ$.

Figure 17.- Continued.

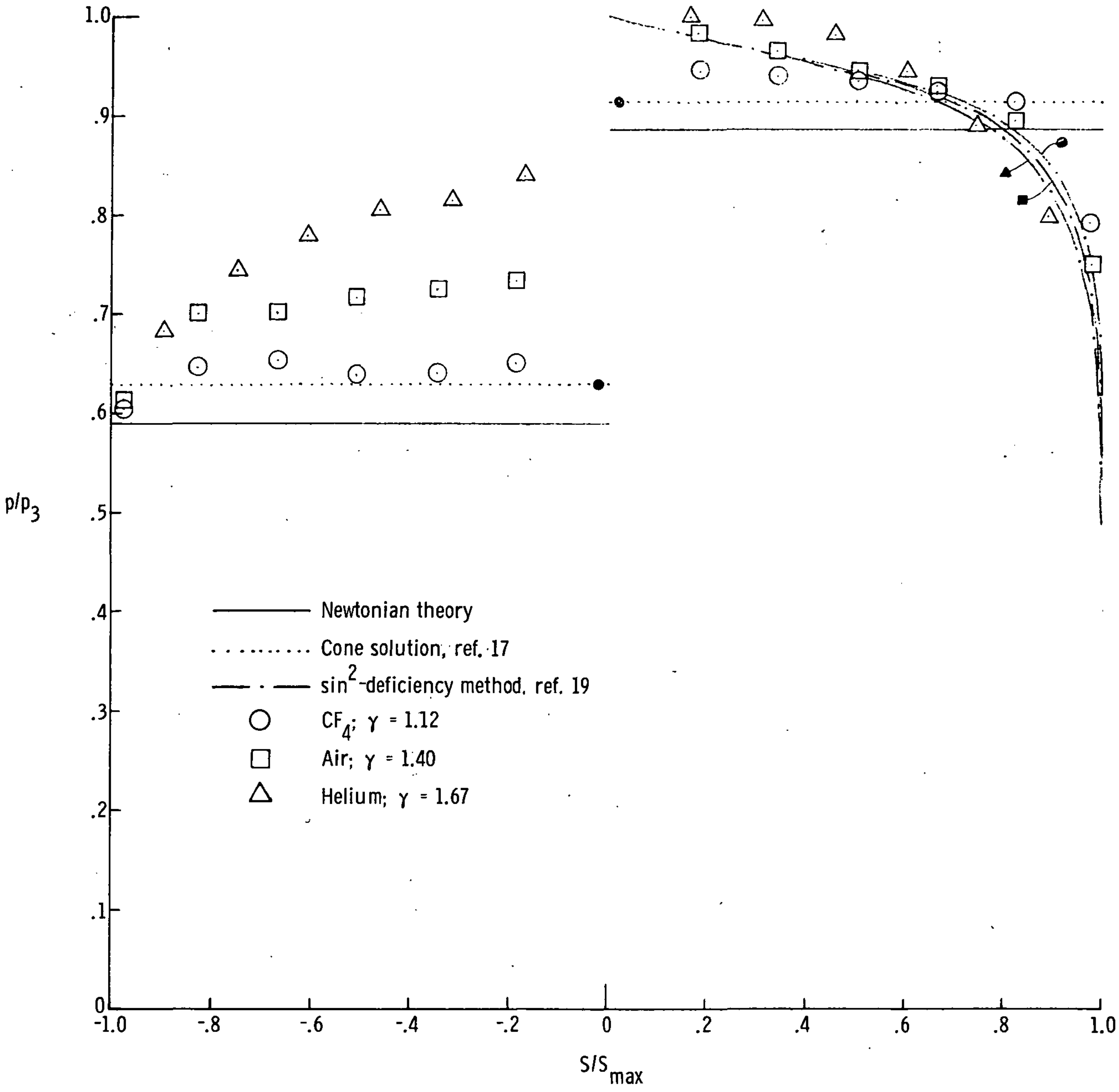

(c) $\alpha = 10^\circ$.

Figure 17.- Continued.

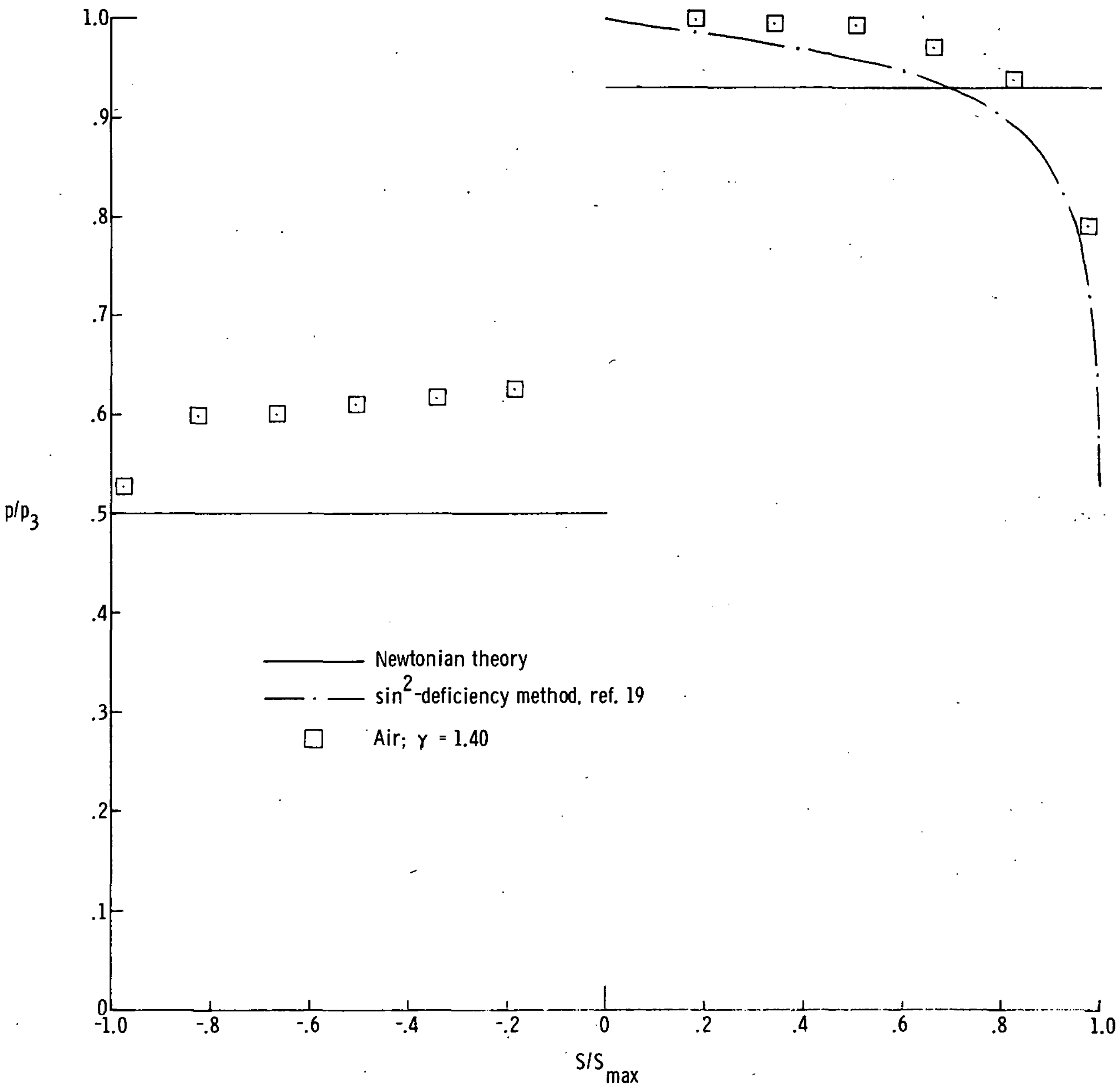

(d) $\alpha = 15^{\circ}$.

Figure 17.- Continued.

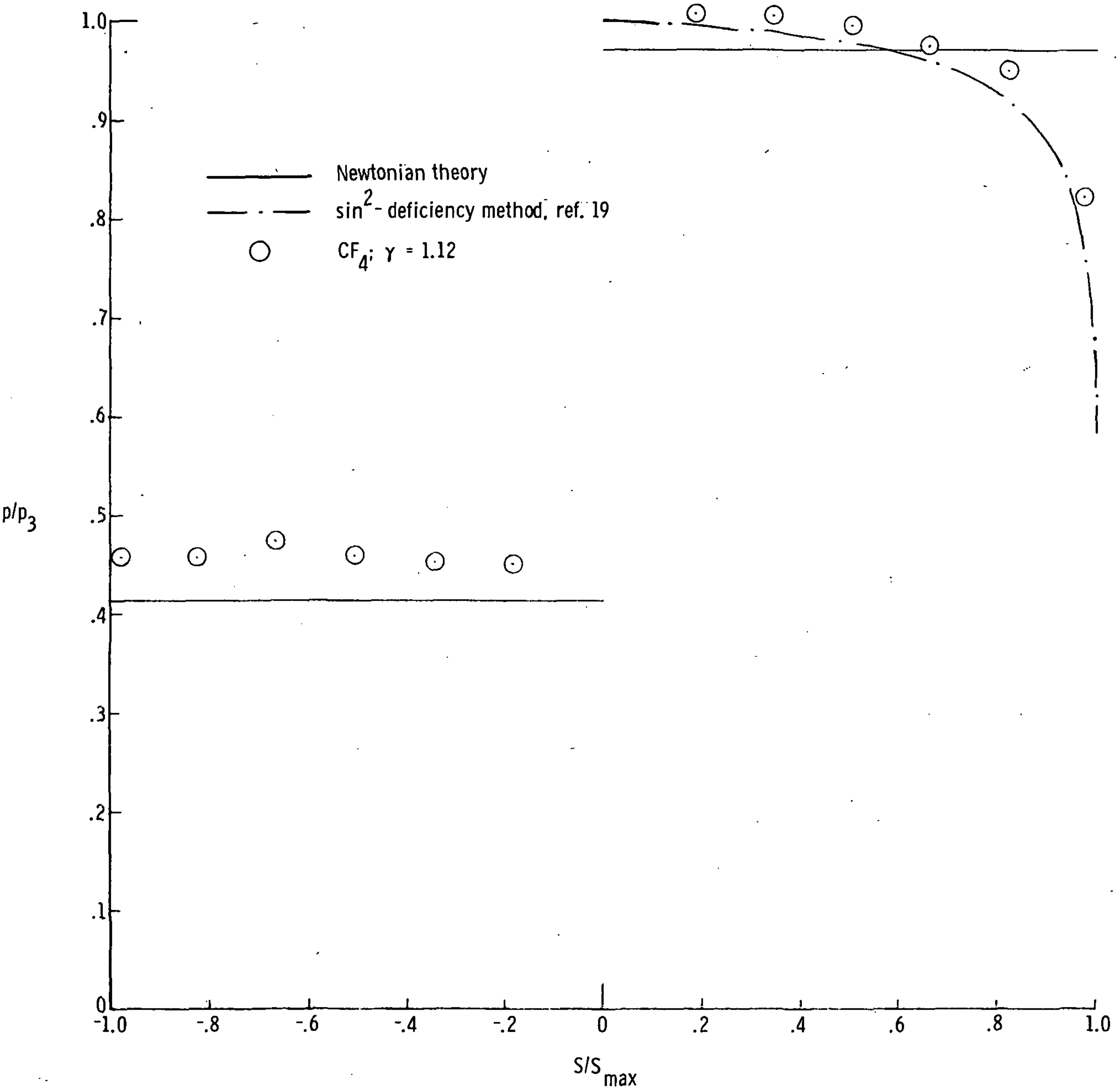

(e) $\alpha = 20^{\circ}$.

Figure 17.- Concluded.

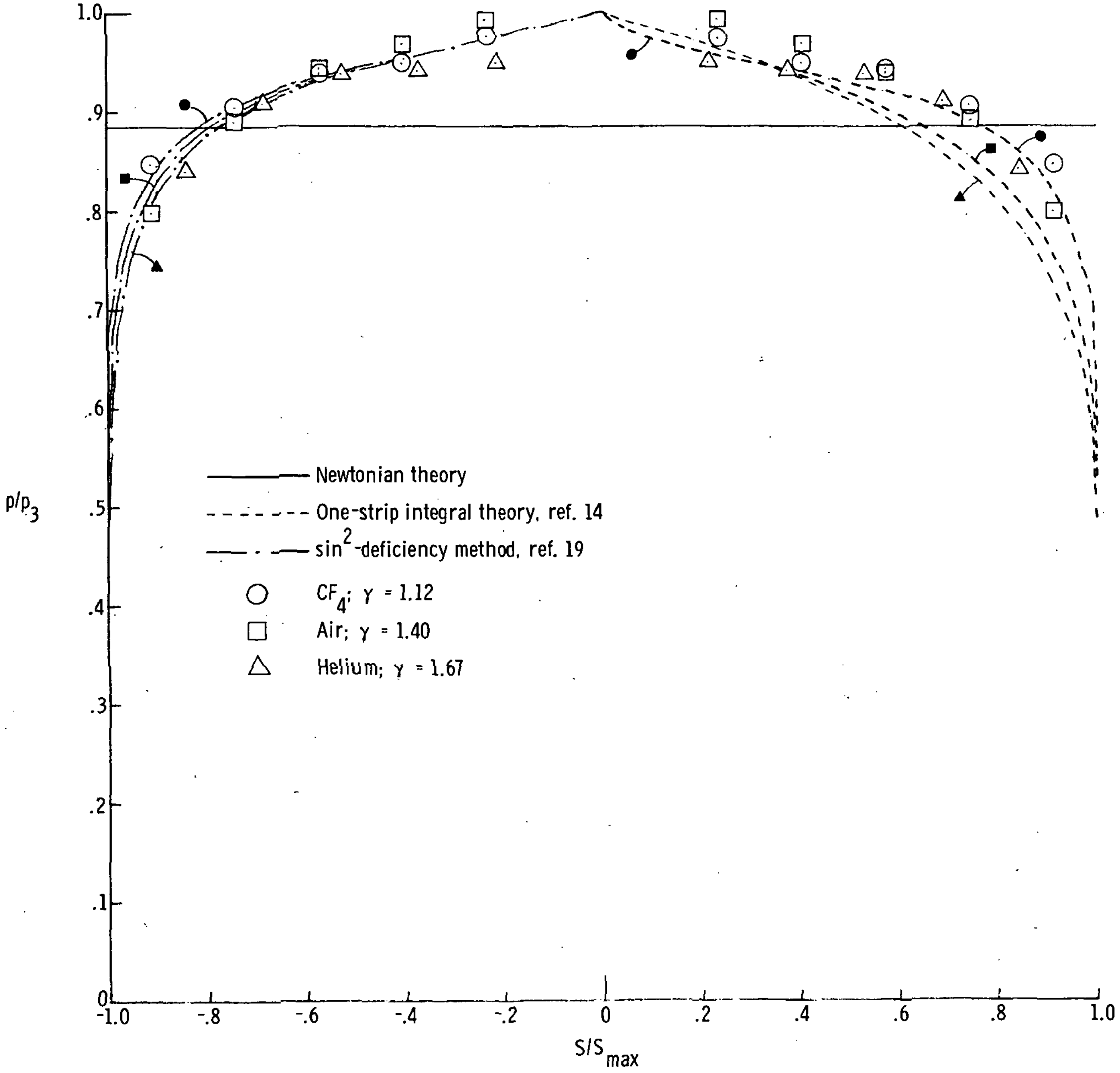

(a) $\alpha = 0^\circ$.

Figure 18.- Pressure distribution on 140° sharp cone.

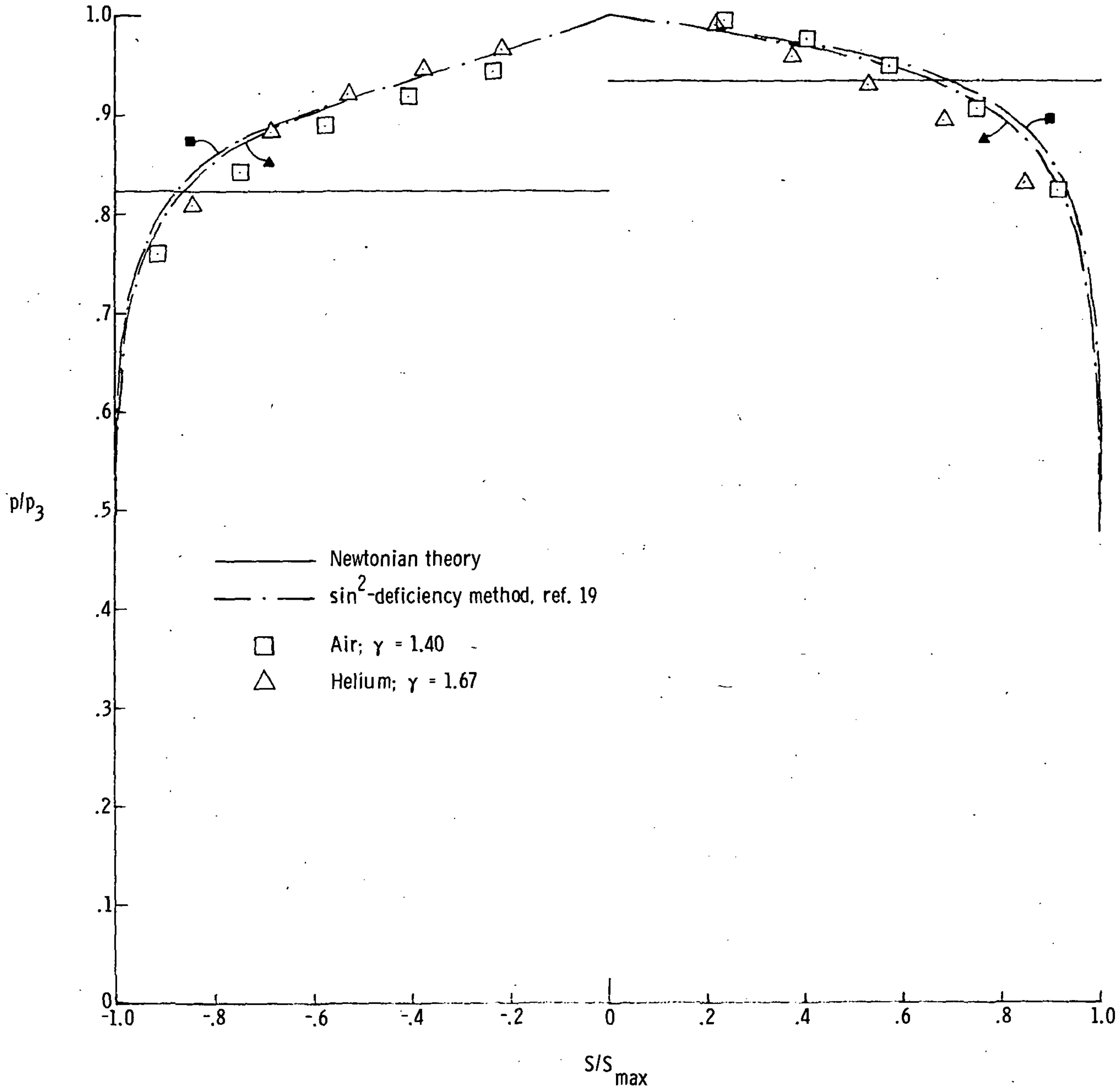

(b) $\alpha = 5^{\circ}$.

Figure 18.- Continued.

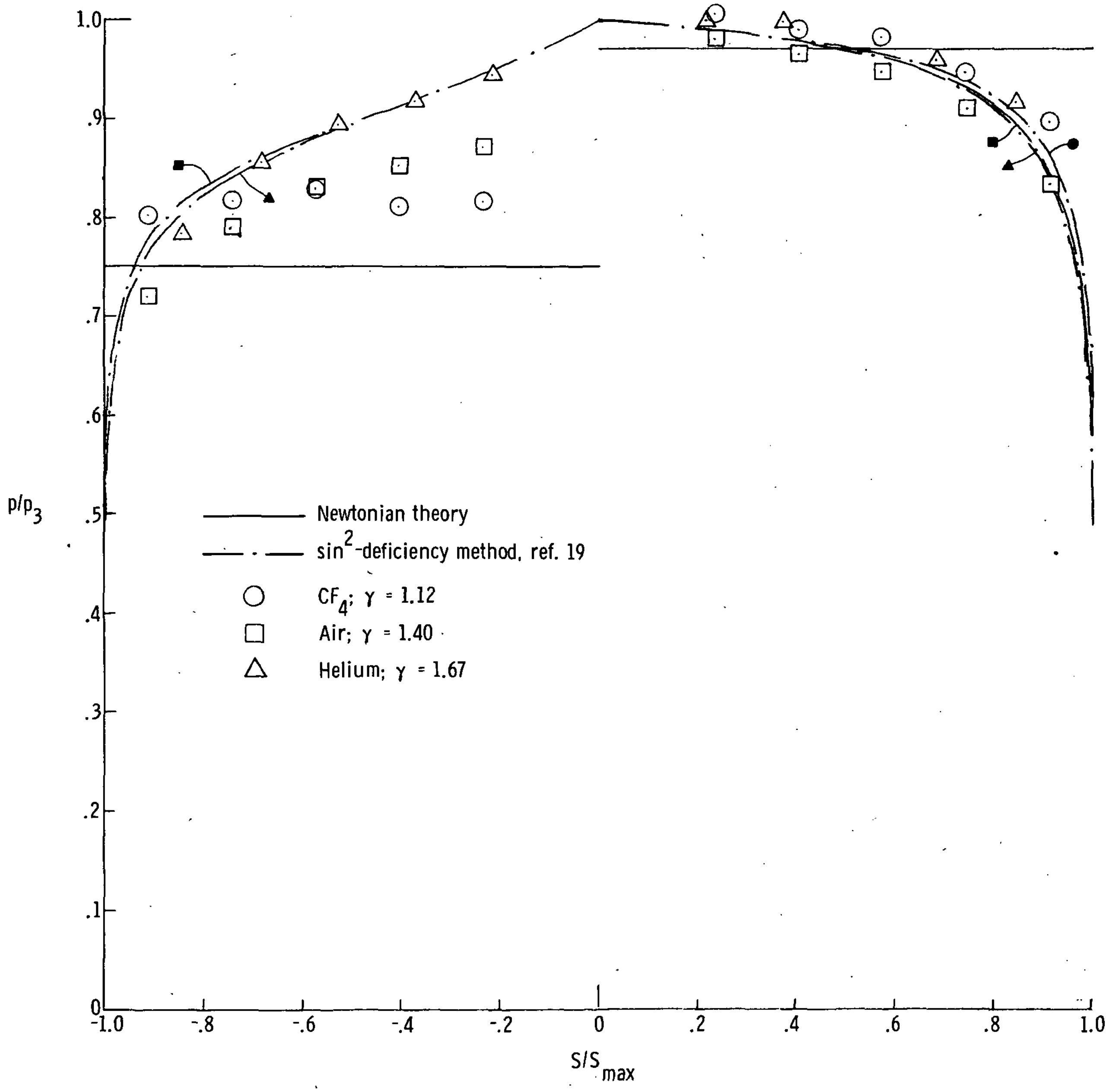

(c) $\alpha = 10^{\circ}$.

Figure 18.- Continued.

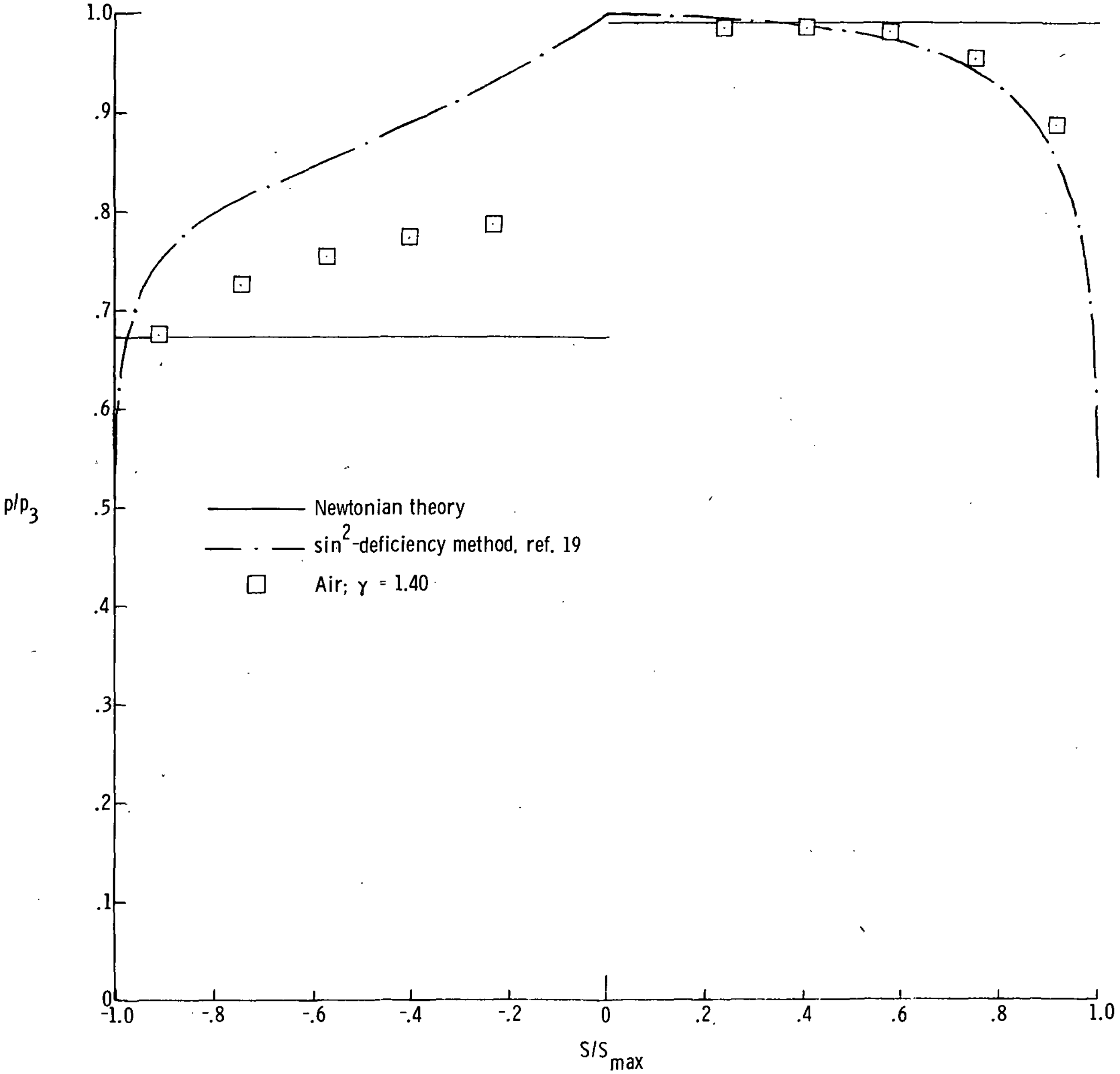

(d) $\alpha = 15^{\circ}$.

Figure 18.- Continued.

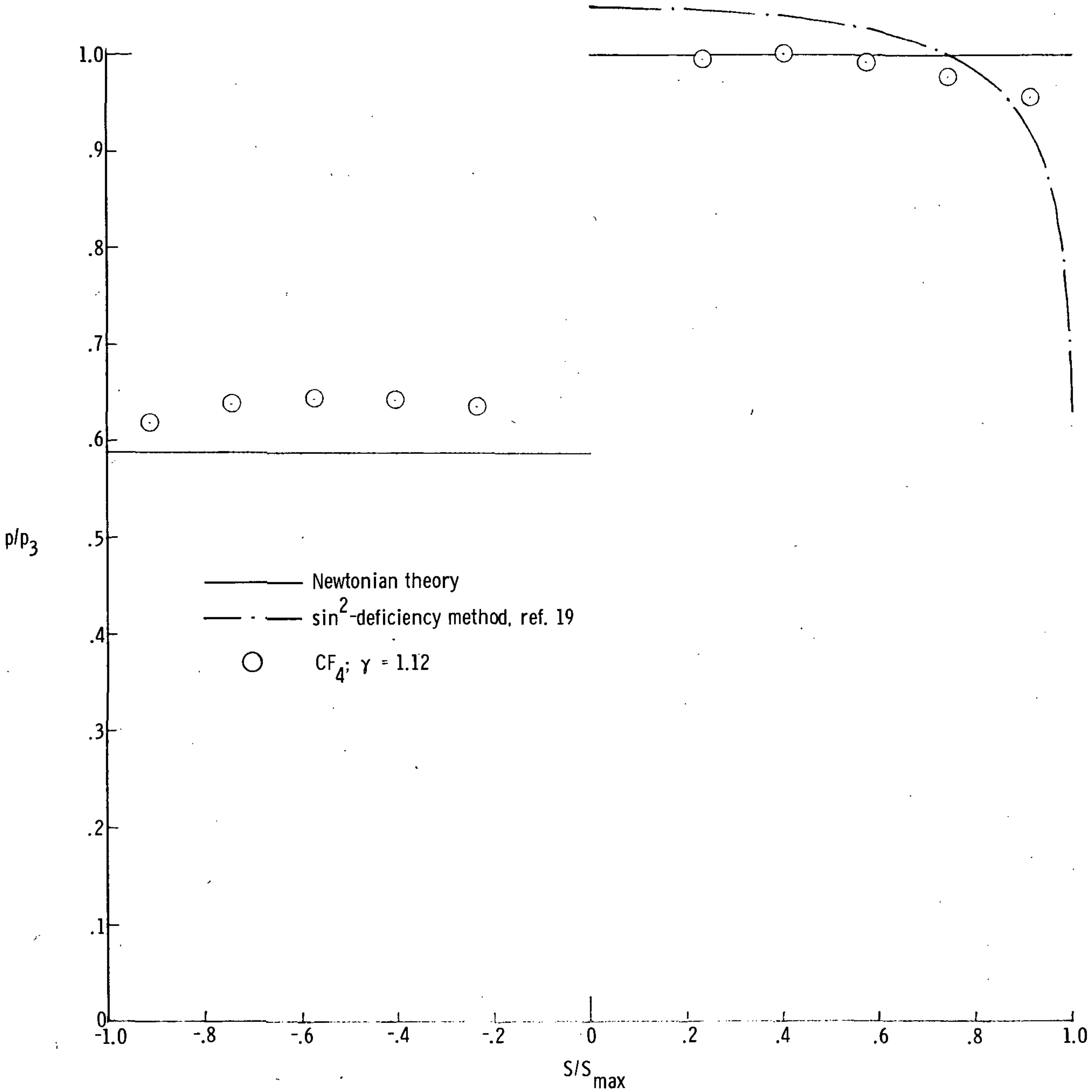

(e) $\alpha = 20^{\circ}$.

Figure 18.- Concluded.

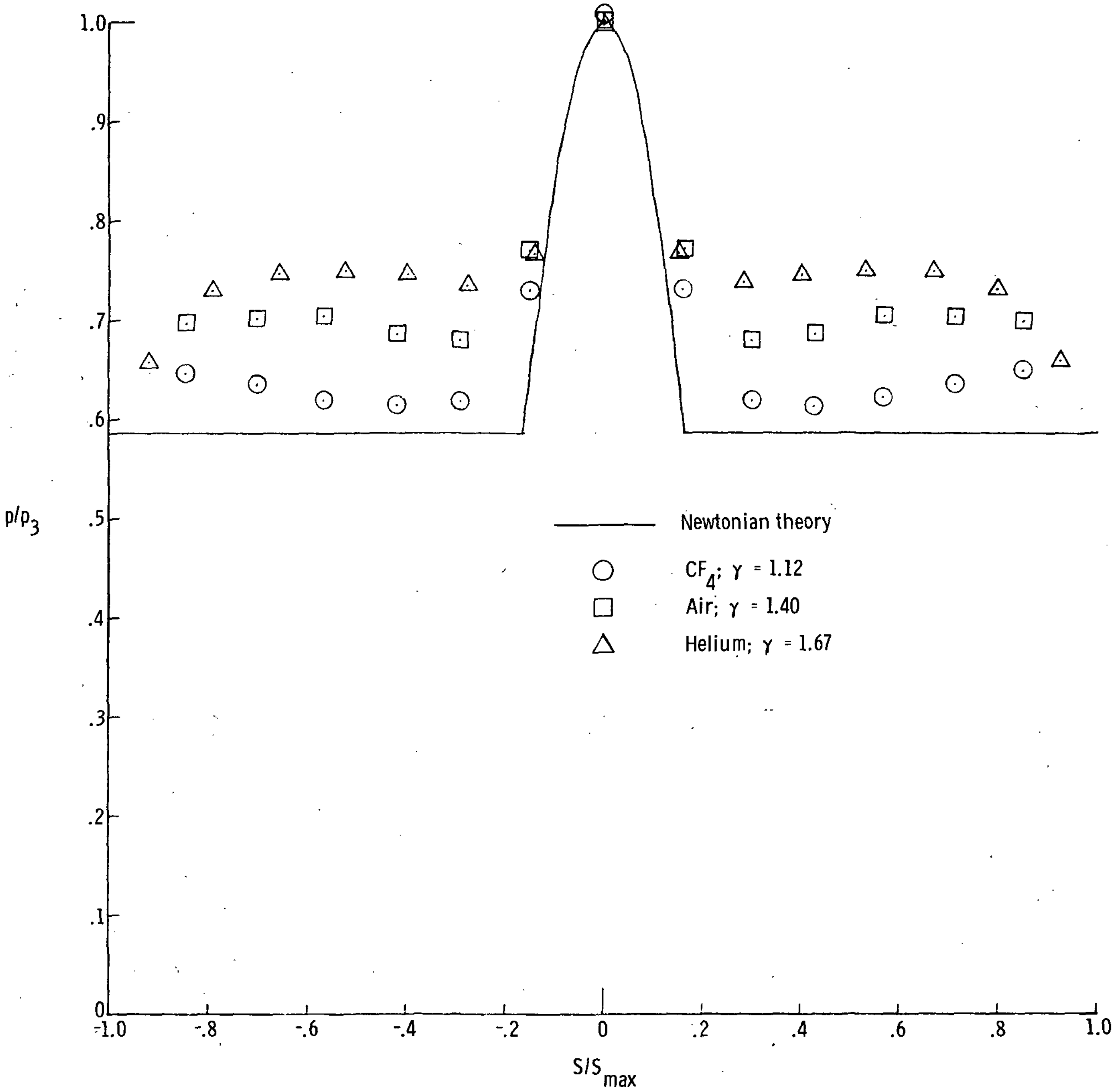

(a) $\alpha = 0^{\circ}$.

Figure 19.- Pressure distribution on 100° blunt cone.

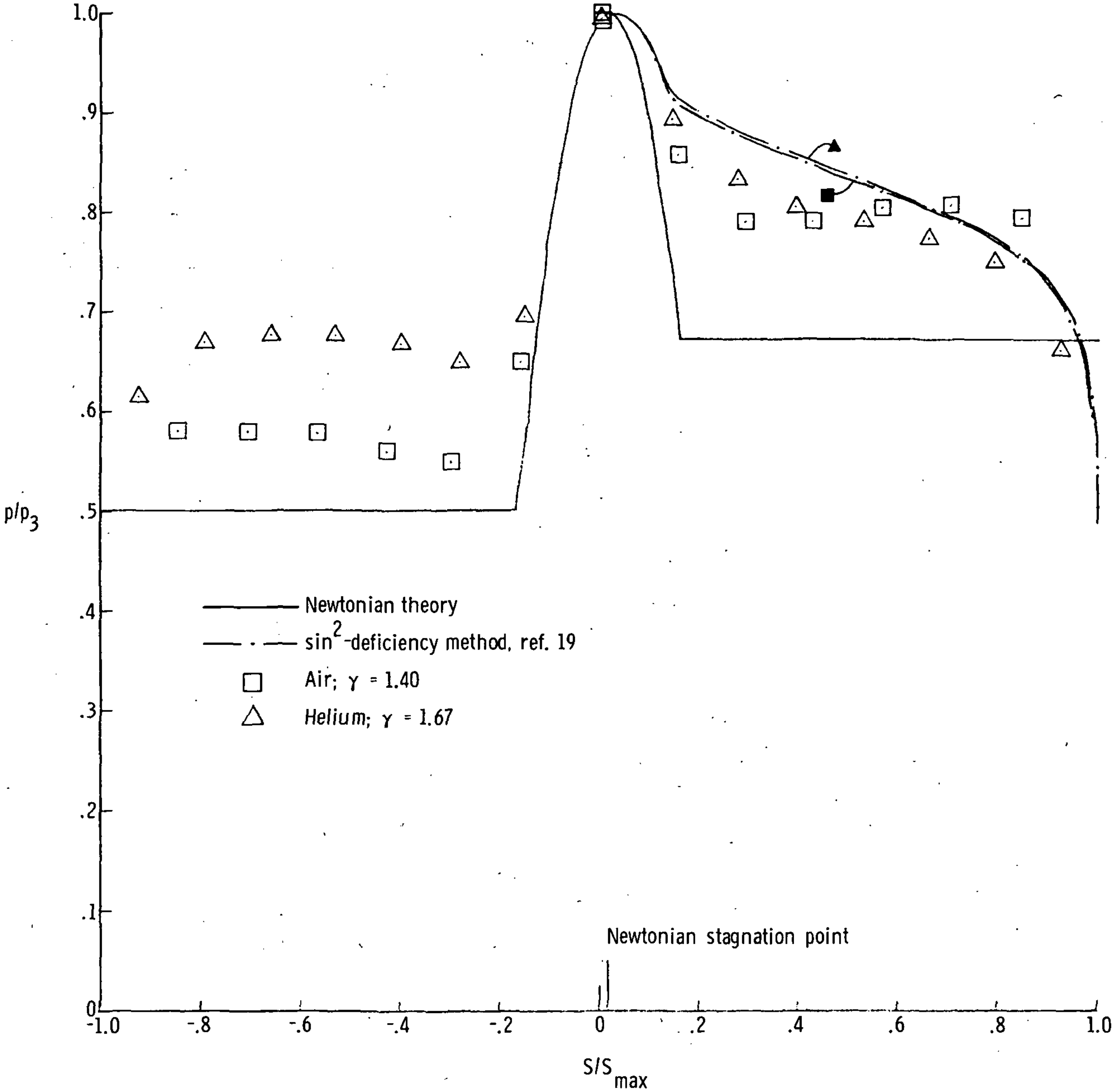

(b) $\alpha = 5^{\circ}$.

Figure 19.- Continued.

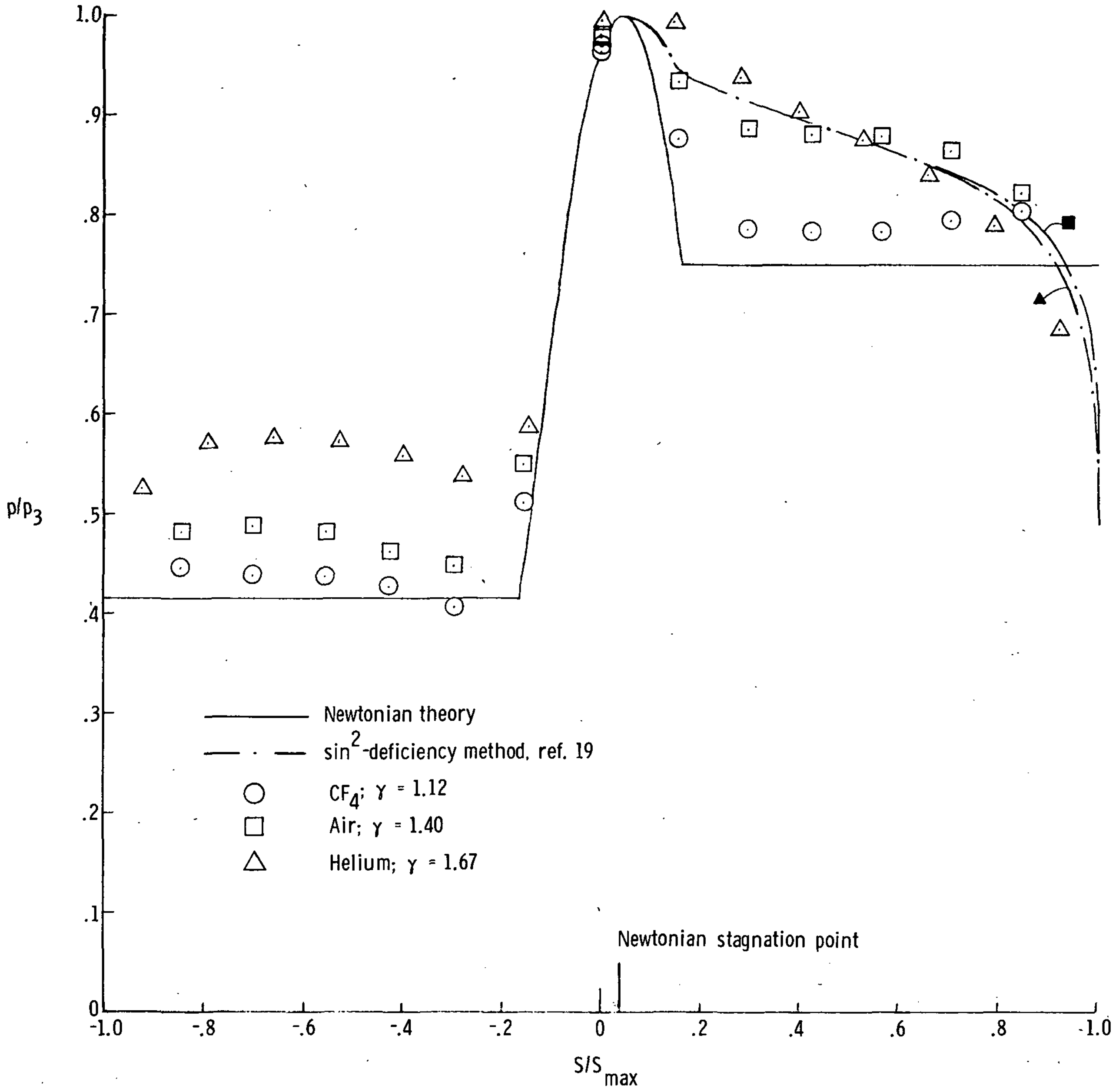

(c) $\alpha = 10^{\circ}$.

Figure 19.- Continued.

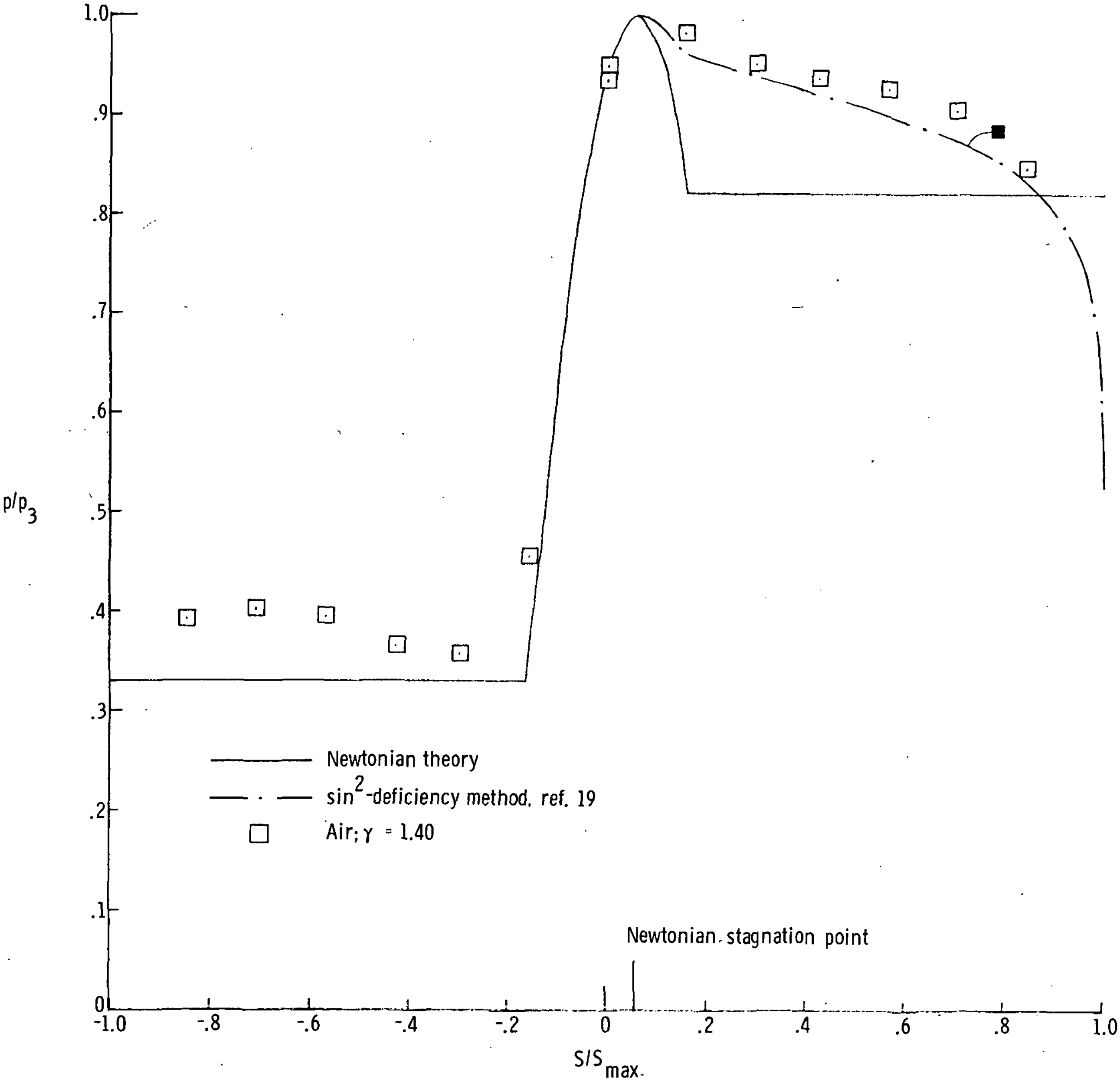

(d) $\alpha = 15^{\circ}$.

Figure 19.- Continued.

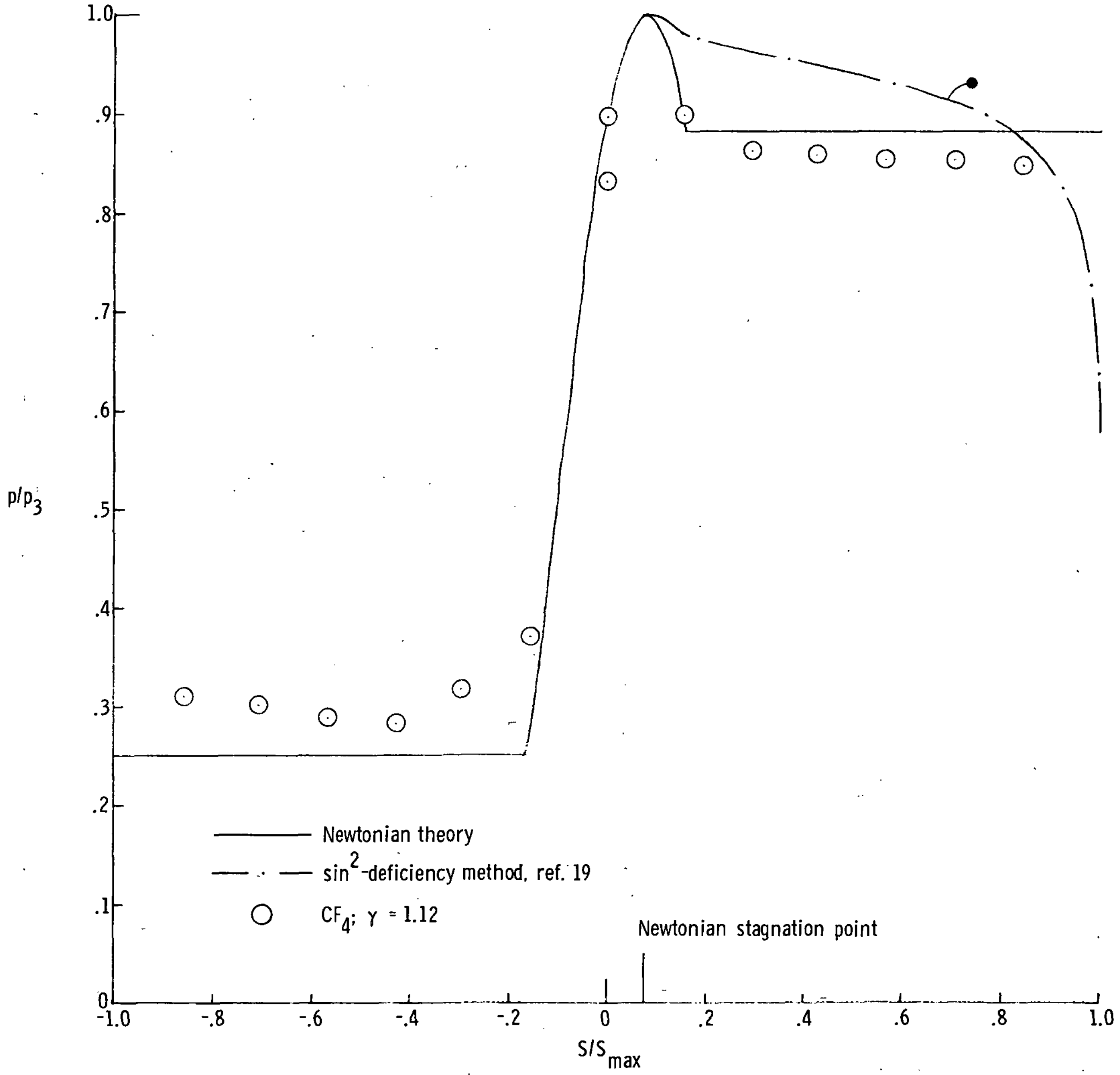

(e) $\alpha = 20^\circ$.

Figure 19.- Concluded.

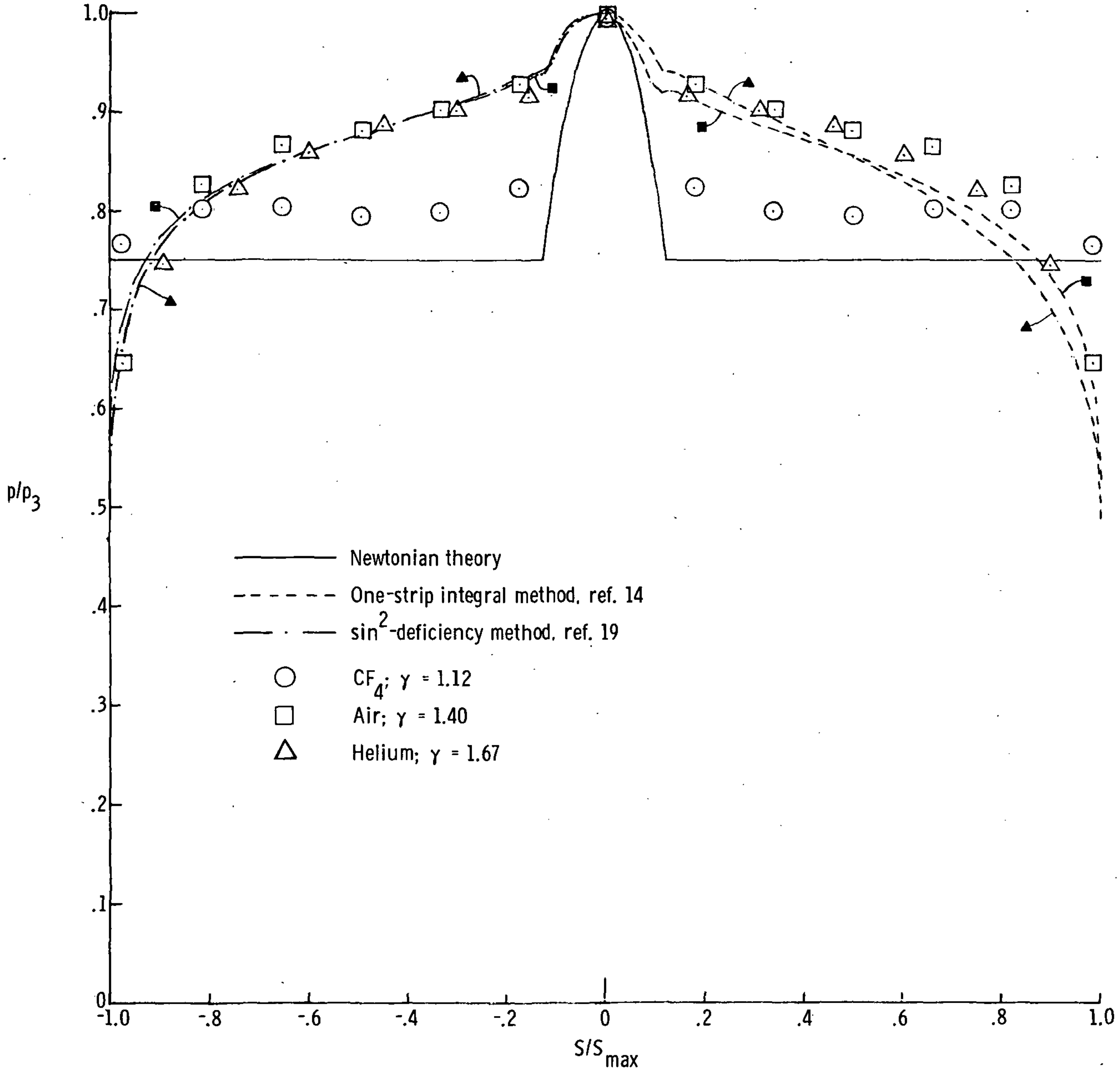

(a) $\alpha = 0^{\circ}$.

Figure 20.- Pressure distribution on 120° blunt cone.

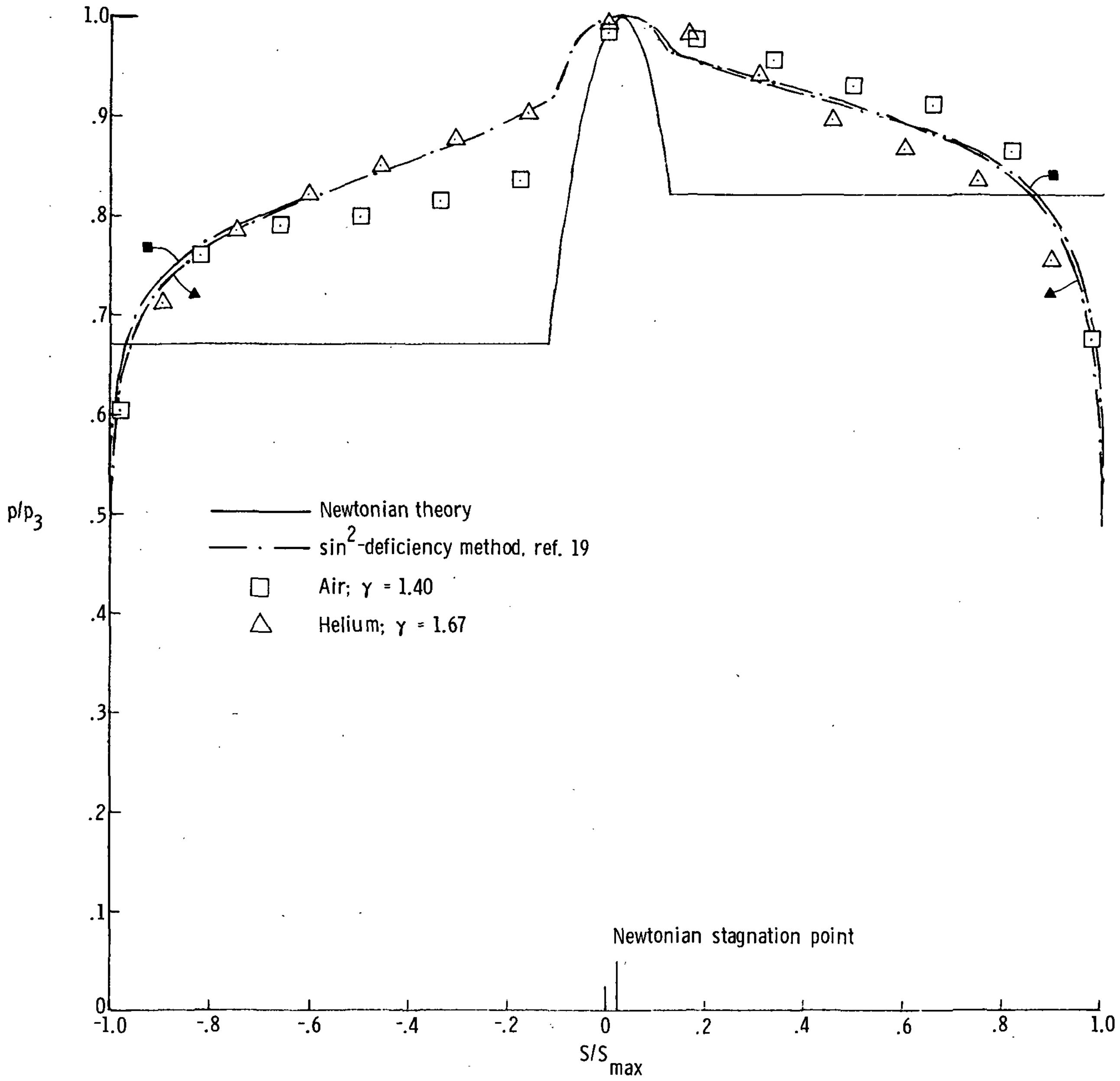

(b) $\alpha = 5^{\circ}$.

Figure 20.- Continued.

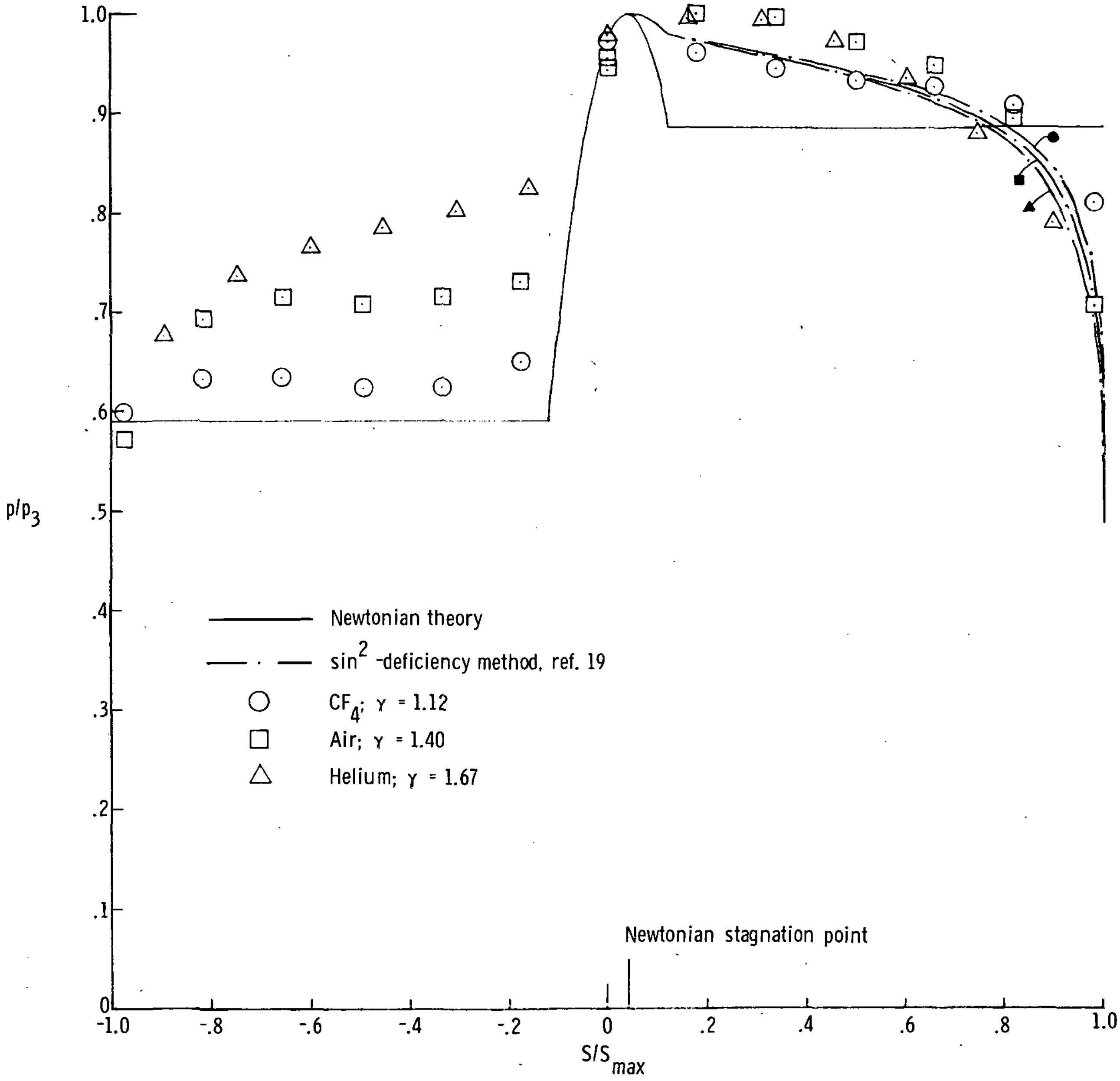

(c) $\alpha = 10^{\circ}$.

Figure 20.- Continued.

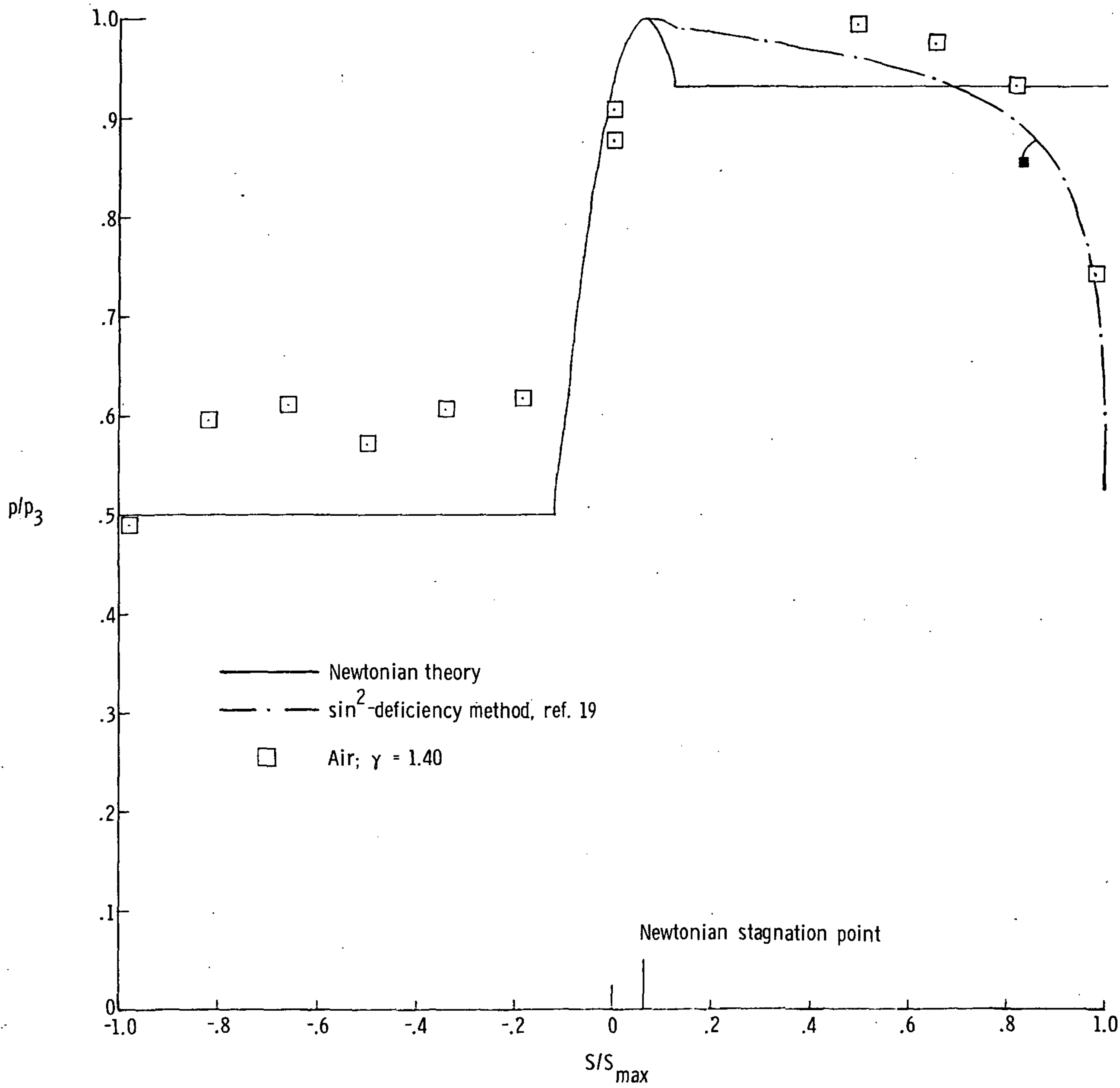

(d) $\alpha = 15^{\circ}$.

Figure 20.- Continued.

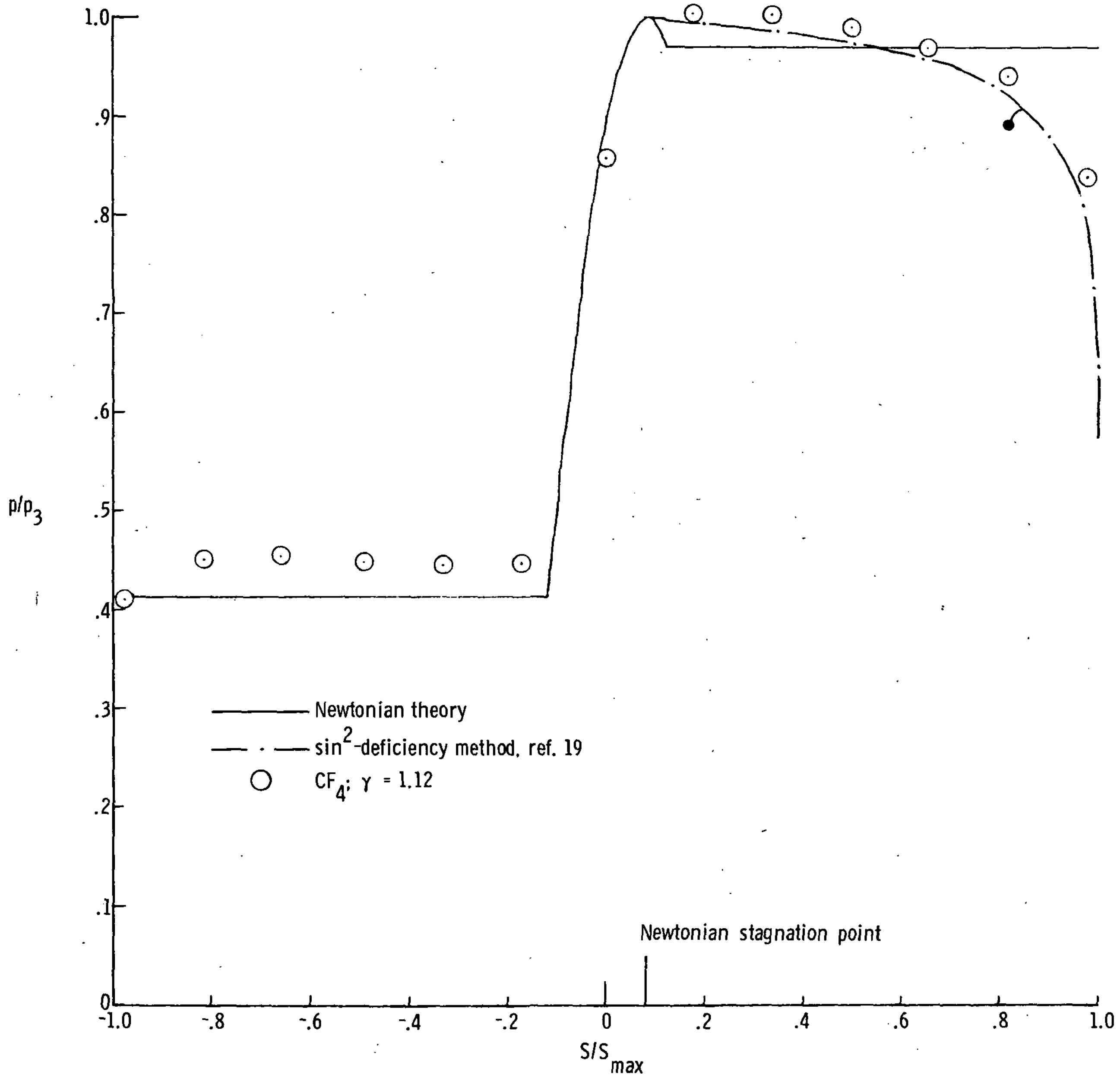

(e) $\alpha = 20^{\circ}$.

Figure 20.- Concluded.

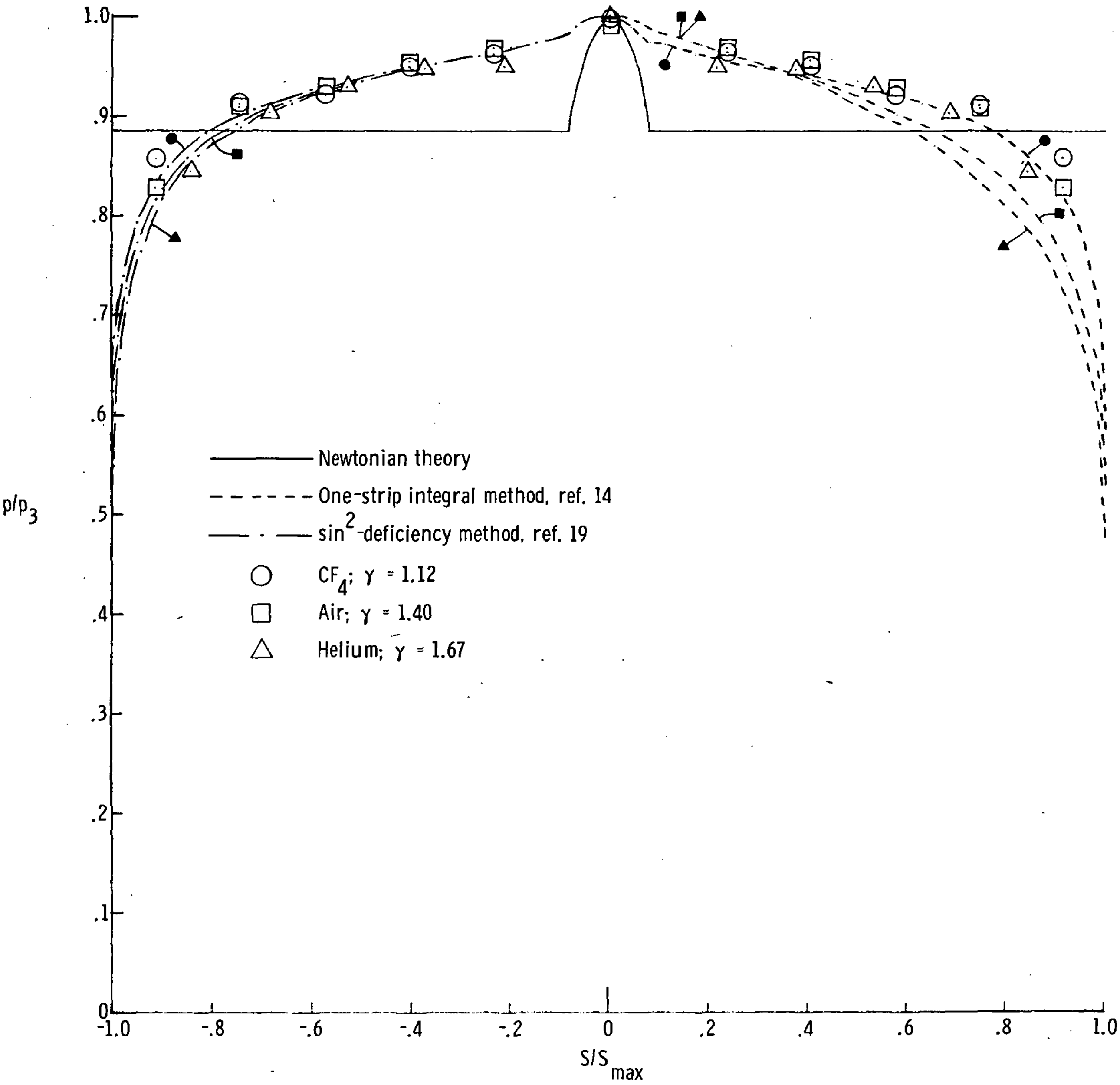

(a) $\alpha = 0^o$.

Figure 21.- Pressure distribution on 140° blunt cone.

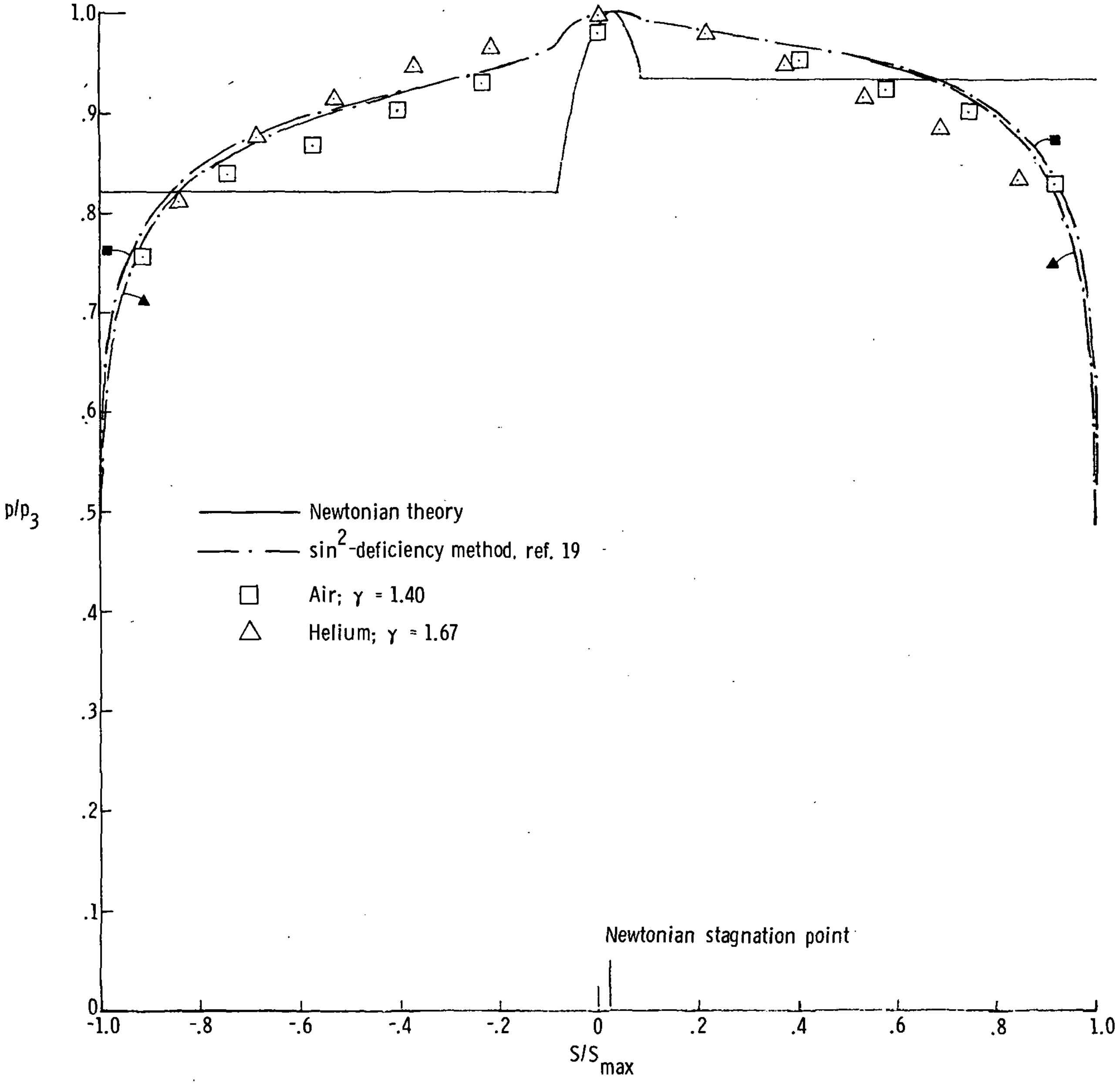

(b) $\alpha = 5^{\circ}$.

Figure 21.- Continued.

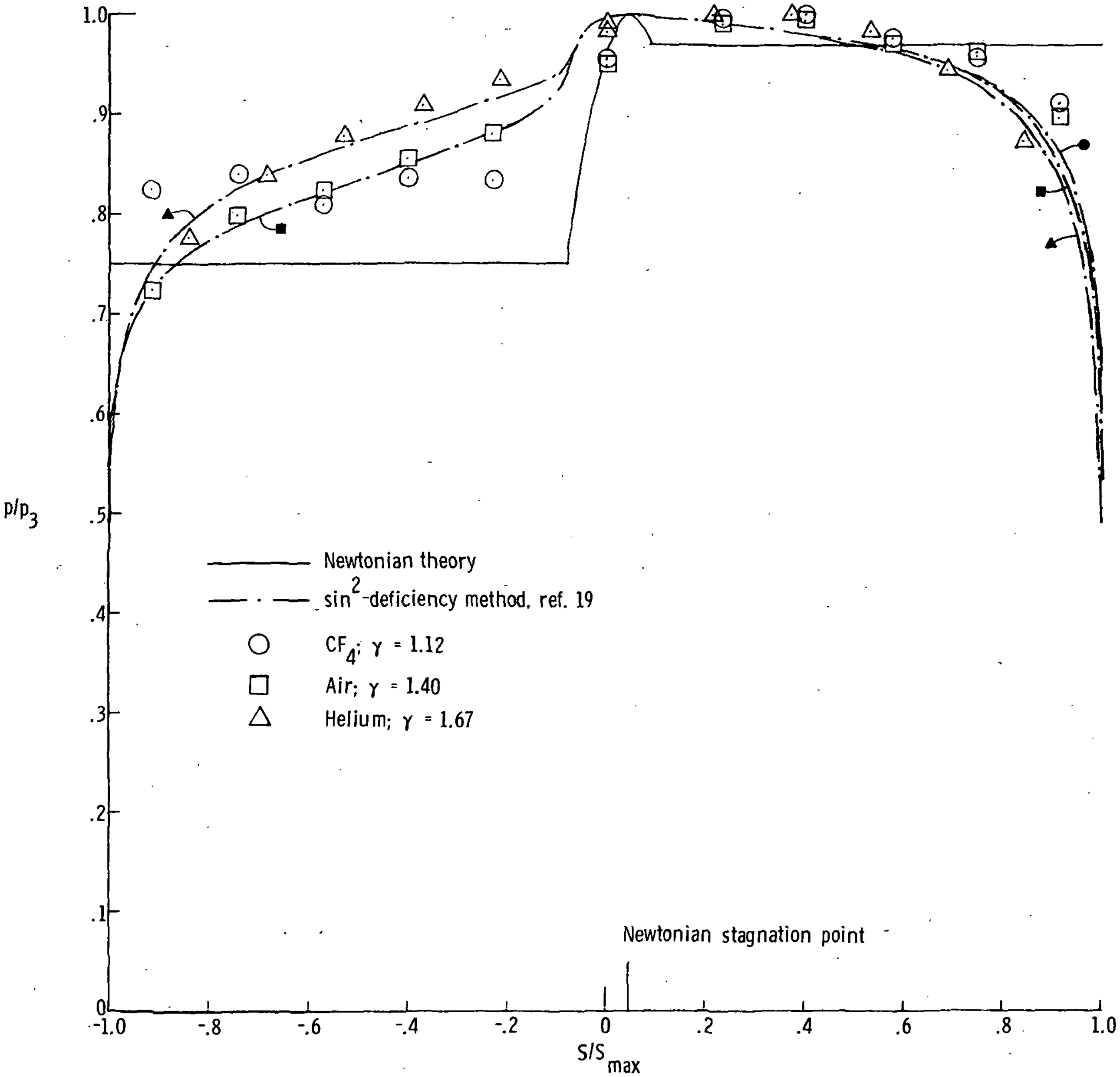

(c) $\alpha = 10^{\circ}$.

Figure 21.- Continued.

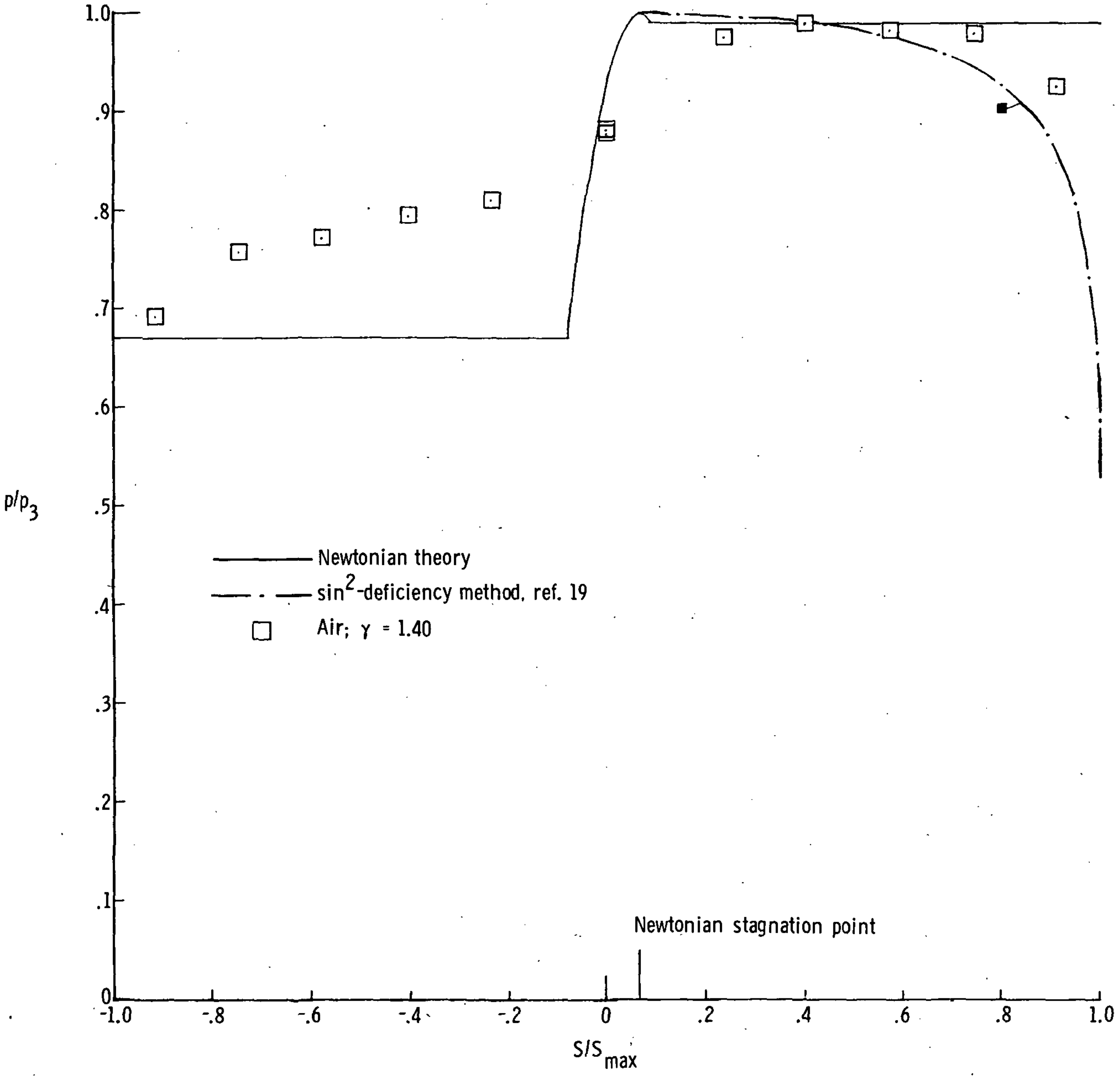

(d) $\alpha = 15^\circ$.

Figure 21.- Continued.

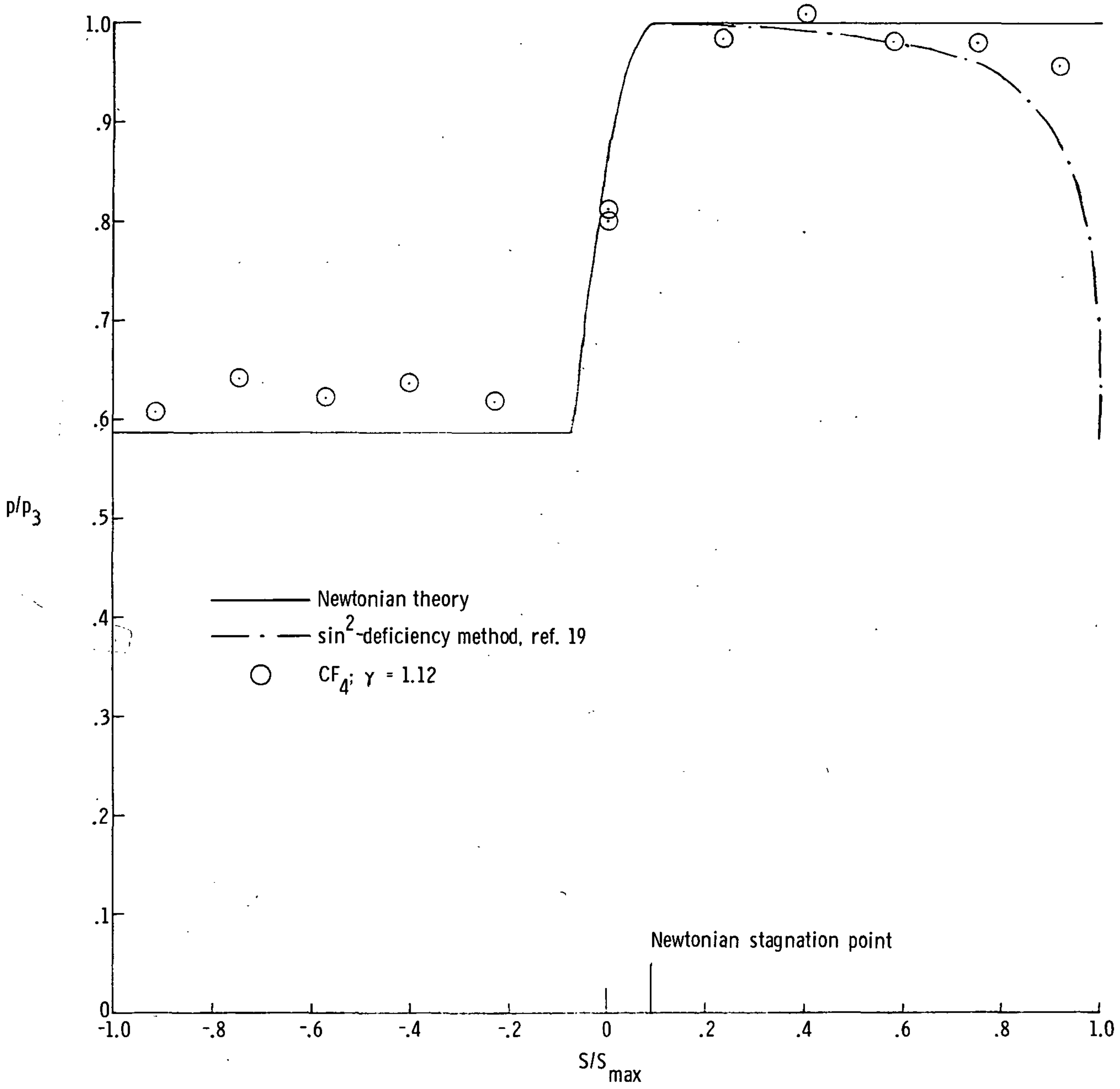

(e) $\alpha = 20^\circ$.

Figure 21.- Concluded.

NASA-Langley, 1973 —— 12 L-8834